

# A combined spectrophotometric and morphometric study of the lunar mare dome fields near Cauchy, Arago, Hortensius, and Milichius

Christian Wöhler<sup>a,\*</sup>, Raffaello Lena<sup>b</sup>, Paolo Lazzarotti<sup>c</sup>, Jim Phillips<sup>d</sup>, Michael Wirths<sup>e</sup>, Zac Pujic<sup>f</sup>,

Geologic Lunar Research (GLR) Group

<sup>a</sup> DaimlerChrysler Research and Technology, Machine Perception, P.O. Box 2360, 89013 Ulm, Germany

<sup>b</sup> Via Cartesio 144, sc. D, 00137 Rome, Italy

<sup>c</sup> Via Pernice 71, 54100 Massa (MS), Italy

<sup>d</sup> 101 Bull Street, Charleston, SC 29401, USA

<sup>e</sup> RR#3 Perth, Ontario, K7H 3C5, Canada

<sup>f</sup> Queensland Brain Institute, The University of Queensland, Queensland 4072, Australia

Received 16 November 2005; revised 7 March 2006

Available online 24 April 2006

## Abstract

In this study we examine the spectral and morphometric properties of the four important lunar mare dome fields near Cauchy, Arago, Hortensius, and Milichius. We utilize Clementine UV–vis multispectral data to examine the soil composition of the mare domes while employing telescopic CCD imagery to compute digital elevation maps in order to determine their morphometric properties, especially flank slope, height, and edifice volume. After reviewing previous attempts to determine topographic data for lunar domes, we propose an image-based 3D reconstruction approach which is based on a combination of photoclinometry and shape from shading. Accordingly, we devise a classification scheme for lunar mare domes which is based on a principal component analysis of the determined spectral and morphometric features. For the effusive mare domes of the examined fields we establish four classes, two of which are further divided into two subclasses, respectively, where each class represents distinct combinations of spectral and morphometric dome properties. As a general trend, shallow and steep domes formed out of low-TiO<sub>2</sub> basalts are observed in the Hortensius and Milichius dome fields, while the domes near Cauchy and Arago that consist of high-TiO<sub>2</sub> basalts are all very shallow. The intrusive domes of our data set cover a wide continuous range of spectral and morphometric quantities, generally characterized by larger diameters and shallower flank slopes than effusive domes. A comparison to effusive and intrusive mare domes in other lunar regions, highland domes, and lunar cones has shown that the examined four mare dome fields display such a richness in spectral properties and 3D dome shape that the established representation remains valid in a more global context. Furthermore, we estimate the physical parameters of dome formation for the examined domes based on a rheologic model. Each class of effusive domes defined in terms of spectral and morphometric properties is characterized by its specific range of values for lava viscosity, effusion rate, and duration of the effusion process. For our data set we report lava viscosities between about 10<sup>2</sup> and 10<sup>8</sup> Pa s, effusion rates between 25 and 600 m<sup>3</sup> s<sup>-1</sup>, and durations of the effusion process between three weeks and 18 years. Lava viscosity decreases with increasing R<sub>415</sub>/R<sub>750</sub> spectral ratio and thus TiO<sub>2</sub> content; however, the correlation is not strong, implying an important influence of further parameters like effusion temperature on lava viscosity.

© 2006 Elsevier Inc. All rights reserved.

**Keywords:** Moon; Volcanism; Image processing; Spectrophotometry; Geological processes

## 1. Introduction

Many theories have been put forward to explain the origin of lunar shields and domes but there is now a general consensus in interpreting most of them as magmatic features, extrusive (volcanic) or intrusive (laccolith) in nature. The geologic processes involved in lunar volcanism were examined in the

\* Corresponding author. Fax: +49 7389 906040.  
E-mail addresses: [christian.woehler@web.de](mailto:christian.woehler@web.de),  
[christian.woehler@daimlerchrysler.com](mailto:christian.woehler@daimlerchrysler.com) (C. Wöhler).

context of the Basaltic Volcanism Study Project (1981) and are also discussed in detail, e.g., by Head and Gifford (1980). Comprehensive overviews are provided by Cattermole (1996) and by Mursky (1996). According to these descriptions, constructional volcanic features formed during the later stages of volcanism on the Moon, characterized by a decreasing rate of lava extrusion and comparably low temperature of eruption, resulting in the formation of effusive domes. Early stage lavas were very fluid due to their high temperatures, massive volumes, and mineralogy. Lunar lavas are mafic in composition (low silica content, high metal oxide content) and tend to have a low viscosity, as opposed to felsic lavas (high silica content), from andesite to rhyolite in composition, which on Earth produce steep-sided domes with short lava flows. Early works by Arthur (1962), Baldwin (1963), and Fielder (1965) have drawn attention to the similarities of lunar domes to terrestrial igneous and volcanic features. The first lavas on the Moon flowed from eruptive fissures and did not produce volcanoes. Across time, the erupting lavas cooled, decreased in flow rate, and began to crystallize so that they began to pile up around the vent through which they effused, forming low shield-like volcanoes. Lower effusion rates due to lower speed of lava uplift and magmatic differentiation may have increased lava viscosity, eventually leading to steeper flank slopes. At that stage, extrusion rates were apparently relatively low, compared to the very high values characteristic for flows associated with major lunar sinuous rilles and terrestrial flood basalts, but may have been relatively high compared to similar terrestrial shields. Large shield volcanoes equivalent to the terrestrial Hawaiian-type do not occur on the Moon. Lack of these features may be due to the low viscosities and high effusion rates typical of many lunar eruptions and the lack of continuous eruptions from single sources (Head and Gifford, 1980; Whitford-Stark and Head, 1977). Many of the lunar effusive domes have a central crater pit, which occurs upon magma withdrawal and subsequent collapse into the vent.

Mare domes differ from distinctive high-albedo domes of volcanic origin located in or near the highlands. The classical examples of highland domes are Gruithuisen  $\gamma$  and  $\delta$ , which have a higher albedo than the nearby Mare Imbrium and also larger diameters and steeper slopes than mare domes. This refers to an early volcanism which was probably unrelated to the lunar maria and was also of different mineralogy (Chevrel et al., 1999). The higher reflectance and spectrally red appearance of these domes supports the assumption of a different mineralogy, which is consistent with lava having a lower FeO and TiO<sub>2</sub> content than mare basalts. It is suggested that the source of this lava is the lower crust, differing from the mare source region, the upper mantle.

A further important type of lunar domes is subsurface intrusions. Here, a subsurface accumulation of magma caused an up-doming of the bedrock layers, creating a smooth, gently sloping structure of positive relief, similar to terrestrial laccoliths (Head and Gifford, 1980; Basaltic Volcanism Study Project, 1981). There are not many good terrestrial analogs to these low swells. The intrusive domes are probably the most poorly understood type of small volcanic structures on the Moon.

Groups of low domes have also been observed on the floor of craters (e.g., Capuanus, Flammarion, Julius Caesar), where the lava was probably trapped under the lens-shaped floor material. The pressure of the intruding lavas found release through controlled passages to the surface and built up domes at these locations.

Lunar domes have been the subject of several geologic studies. The extended field of lunar domes and cones situated near the crater Marius in central Oceanus Procellarum has been examined in terms of stratigraphy (Dunkin and Heather, 1999) as well as dome and cone morphology and spectral properties (Weitz and Head, 1999). Similar studies have been undertaken for the Rümker dome complex in northern Oceanus Procellarum (Smith, 1974; Weitz and Head, 1999). The Rümker domes are mare domes, given their size and morphology, while the Marius domes and cones are different from typical mare domes due to their complex structure, indicating a formation in several stages involving different eruption styles and lava compositions (Head and Gifford, 1980; Whitford-Stark and Head, 1977). Further important fields of typical lunar mare domes are situated in western and northern Mare Tranquillitatis near the craters Arago and Cauchy, respectively, and in eastern Oceanus Procellarum near the craters Hortensius and Milichius.

A classification scheme for lunar mare domes, relying on their morphology and rough estimates of diameter and flank slope, has been devised by Head and Gifford (1980). Pike (1978) performed a comparative statistical analysis of the morphometric properties of volcanoes on the Earth, the Moon, Mars, and Venus, but his data set includes only five lunar domes. The lunar topographic orthophotomaps acquired by the Apollo 15, 16, and 17 command modules with modified aerial cameras were computed based on classical photogrammetric triangulation and represent the highest-resolution lunar topographic data currently available with elevation standard errors of 30 m (Greeley and Batson, 1990). They only cover a small portion of the lunar surface, including Mare Serenitatis and Mare Tranquillitatis. Pike and Clow (1981) have used this set of topographic maps to determine the heights of various volcanic edifices, including several lunar cones near Aristarchus and in Mare Serenitatis and the mare dome Cauchy  $\omega$  in Mare Tranquillitatis. Except Cauchy  $\omega$ , however, the mare domes situated in the regions covered by these maps are too low to appear in them. The Hortensius and Milichius dome fields are not included by the lunar topographic orthophotomaps.

The Clementine spacecraft performed a topographic mapping of the complete lunar surface at a resolution of 0.25° in longitude and latitude, i.e., better than 7.5 km, by means of laser altimetry. Although the obtained topographic data show large-scale features such as the huge South Pole Aitken Basin on the lunar far side, they do not reveal the 3D structure of the lunar surface on small, e.g., kilometer, scales. Hence, lunar mare domes are too small to appear in the Clementine laser altimeter maps (Bussey and Spudis, 2004).

Images of the Clementine spacecraft have been used to derive topographic maps of the lunar polar regions by stereophotogrammetry (Cook et al., 1999). This approach is feasible since

these regions are always observed under oblique illumination, leading to a sufficient amount of image structure to establish point-to-point correspondences between image pairs. A state-of-the-art multi-image shape from shading method has been applied to Clementine images of the polar regions in order to obtain topographic data, again made possible by the oblique illumination conditions (Lohse and Heipke, 2003). The method makes use of image pairs acquired under virtually identical incidence angles but different emission angles. It exploits the comparably weak influence of emission angle on image brightness under oblique illumination rather than the strong influence of incidence angle (cf. Section 4.2). Hence, it requires accurate knowledge about the reflectance function of the examined lunar surface parts and a precise absolute radiometric calibration of the image data. What is more, the algorithm requires a very good initialization, which is obtained based on stereophotogrammetry. Hence, it is only suitable for strongly cratered or textured surfaces regions, which is generally not the case for surfaces of lunar mare domes.

Determination of height by classical shadow analysis is difficult for lunar domes due to their shallow slopes. It is only possible at solar altitudes which are lower than the flank slopes, such that it is essentially unfeasible using Lunar Orbiter and Clementine imagery. Brungart (1964) determined the heights of more than 100 lunar domes based on images of the othographic lunar atlas (Kuiper, 1961) by measuring shadow lengths, but we will show in this study that his height estimates tend to be systematically too high. A possible reason is that on the high-contrast photographic reproductions of that time true shadows and shading effects could easily be confused.

Photoclinometric and shape from shading techniques (Wilhelms, 1964; McEwen, 1985; Horn, 1989) are suitable for the 3D reconstruction of small regions on the lunar surface. They cannot be applied, however, to Lunar Orbiter or consolidated lunar atlas (Kuiper et al., 1967) images due to the lack of radiometric calibration of the corresponding image data. Wöhler and Hafezi (2005) have demonstrated the applicability of shape from shading methods to the 3D reconstruction of shallow lunar volcanic constructs, relying on telescopic CCD imagery. A corresponding systematic investigation of a larger set of lunar mare domes, however, has not been undertaken so far.

In this study we will thus perform morphometric analyses of lunar mare domes from the Cauchy, Arago, Hortensius, and Milichius dome fields based on high-resolution telescopic CCD imagery. These will be complemented by an investigation of the spectral properties of the mare basalts out of which the domes are formed, relying on Clementine UV-vis spectrophotometry. Furthermore, we will devise a classification scheme for lunar mare domes which is complementary to the scheme introduced by Head and Gifford (1980) in that it is based on the corresponding quantities rather than largely qualitative morphologic considerations. We will discuss how factors like effusion rate and lava mineralogy, especially metal oxide content, with their influence on lava viscosity, may have controlled the observed sizes and shapes of lunar mare domes.

## 2. Geologic setting of the examined dome fields

Different mare units are usually distinguished and mapped according to their spectral properties, which are related to compositional differences. Subsequently, crater counts are performed within these spectrally homogeneous units in order to determine their ages (Hiesinger et al., 2003). The earliest lavas, which erupted during the main phase of mare volcanism, were high-TiO<sub>2</sub> basalts in Mare Tranquillitatis and Mare Serenitatis between 3.8 and 3.6 Ga, according to the basalt samples returned by the Apollo 11 and 17 missions, respectively. Lower-TiO<sub>2</sub> basalts were erupted between about 3.6 and 3.1 Ga in Mare Crisium and Fecunditatis (Luna 16 and 24 sample-return missions), Mare Imbrium (3.3 Ga, Apollo 15), and Oceanus Procellarum (3.1 Ga, Apollo 12). Still younger flows may be about 2.0 Ga old, represented by portions of Mare Imbrium and the Surveyor 1 landing site in Oceanus Procellarum situated within the lava-filled crater Flamsteed P. These basalts probably erupted during one of the latest stages of lunar volcanism. They have been mapped as Eratosthenian in age while the surrounding mare units are likely Imbrian (Wilhelms, 1987; Melendrez et al., 1994). Geologic maps of the four examined lunar dome fields are shown in Fig. 1.

Two dome fields examined in this study are situated in Mare Tranquillitatis, in proximity of the craters Cauchy and Arago, respectively (Fig. 2). Mare Tranquillitatis lies on the site of an ancient and large basin, irregular in outline, formed by a major impact during the pre-Nectarian time. This basin has been flooded by basaltic lavas whose ages are ranging from 3.8 to 3.3 Ga, mapped as Upper Imbrian by Wilhelms (1987). Composition and stratigraphy of the basaltic lavas in Mare Tranquillitatis have been extensively studied (Staid et al., 1996; Rajmon and Spudis, 2001). In the region around the 12 km crater Cauchy in north-eastern Mare Tranquillitatis, the well-known tectonic features Rima Cauchy (a graben) and Rupes Cauchy (a fault) are situated. Several domes are apparent along the extension of Rupes and Rima Cauchy, which are in turn oriented radially to the Imbrium basin. Domes associated with a graben along a strike are interpreted to be formed by very shallow dikes (Petrycki and Wilson, 1999). Rima Cauchy and the nearby domes lie within a topographically high region of high-TiO<sub>2</sub> basalts that appears strongly blue in Clementine color ratio data; the eastern part of the Tranquillitatis basin lies higher than the western part (Staid et al., 1996). Wilhelms and McCauley (1971) have mapped the domes in the Cauchy region as Eratosthenian–Imbrian in age in an area of Imbrian age basalts.

Arago is an Eratosthenian crater located in the western part of Mare Tranquillitatis. To the north of Arago the large lunar dome Arago  $\alpha$  is situated. The similar-sized dome Arago  $\beta$  is located to the west. Arago  $\alpha$  and  $\beta$  have irregular profiles showing protrusions and possible eruptive vents. Between Arago  $\alpha$  and the crater Maclear three well-known aligned and very shallow domes with diameters between 5 and 8 km can be found. These domes have formed in basalts of very high TiO<sub>2</sub> content, and they appear strongly blue in the Clementine UV-vis color ratio image (Fig. 2f). The domes Arago  $\alpha$  and  $\beta$  are slightly less

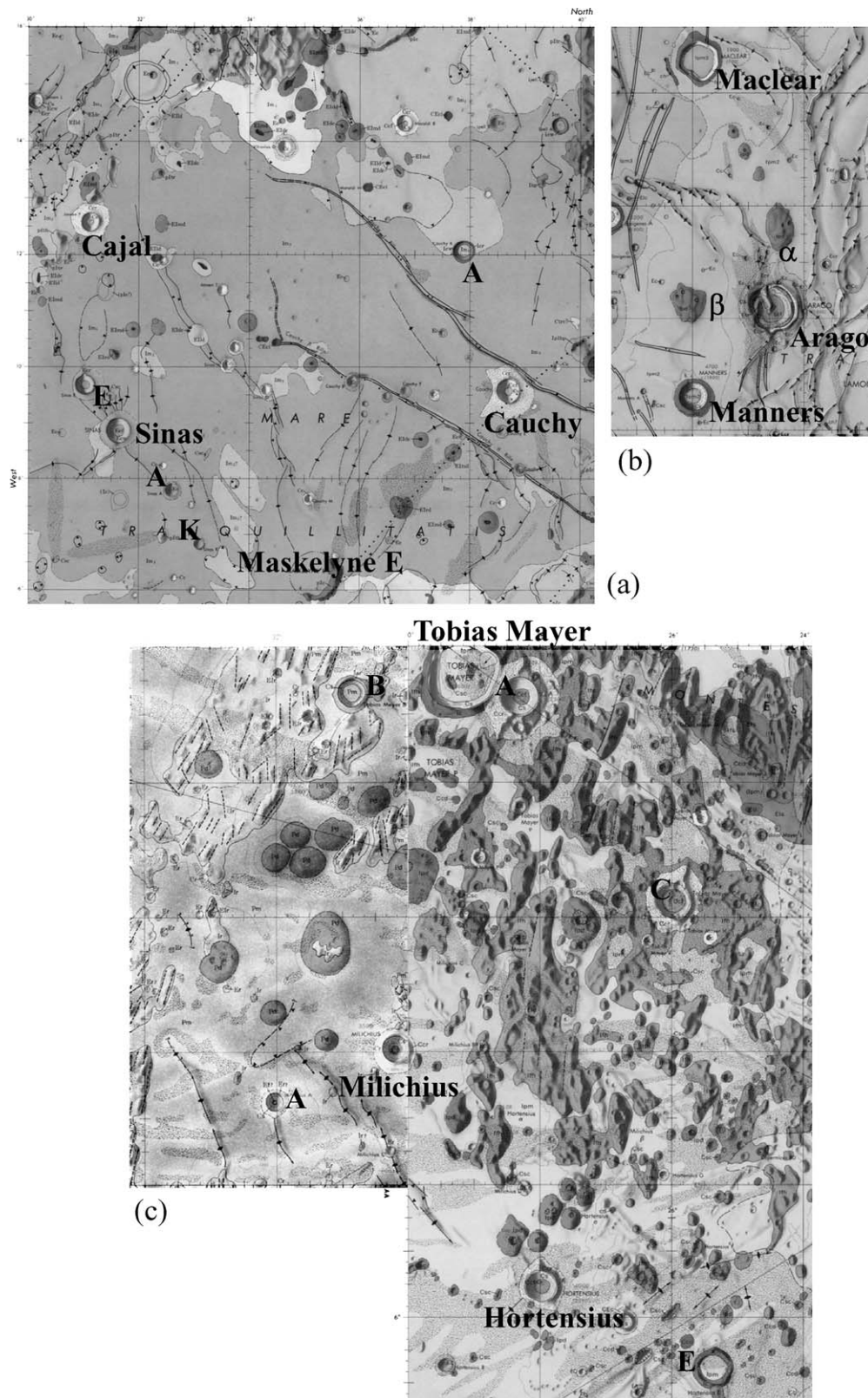


Fig. 1. (a) USGS geologic map I722 of the region around Cauchy. (b) USGS geologic map I510 of the region around Arago. (c) USGS geologic maps I515 and I355 of the regions around Hortensius and Milichius.

blue, and Arago  $\alpha$  is spectrally somewhat redder than the surrounding mare basalts, such that it may be possible that it has been embayed by a layer of younger basalt richer in  $\text{TiO}_2$ .

Stratigraphic relations described by Rajmon and Spudis (2001) support the idea that magmatic activity in Mare Tranquillitatis started with low- $\text{TiO}_2$  lavas and gradually changed

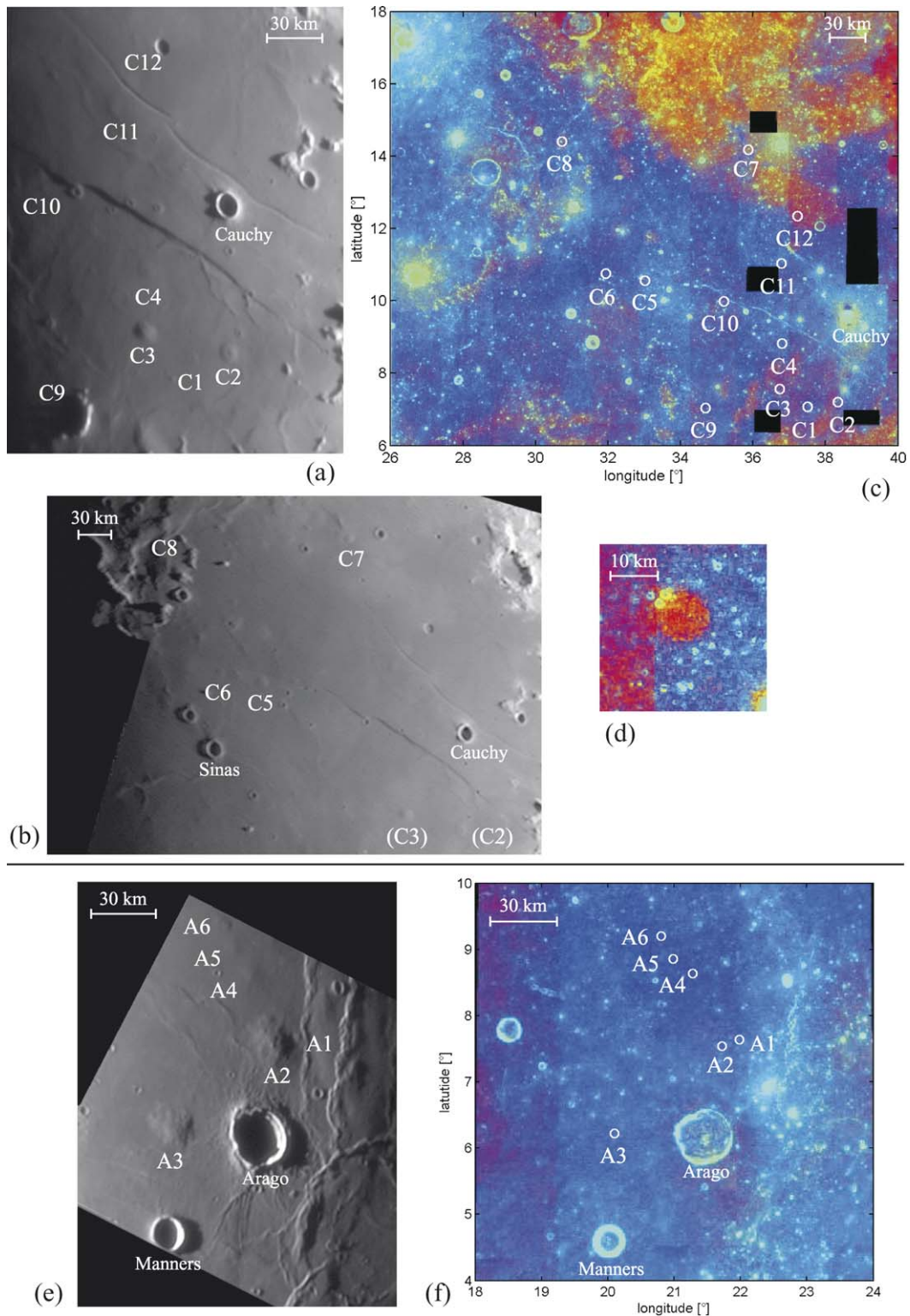


Fig. 2. Telescopic CCD images of (a) the dome field around Cauchy and (b) the domes in northern Mare Tranquillitatis. (c) Clementine UV-vis ratio image, indicating the locations of the examined domes.  $R_{750}/R_{415}$  is denoted by the red,  $R_{750}/R_{950}$  by the green, and  $R_{415}/R_{750}$  by the blue color channel, respectively. (d) UV-vis ratio image of dome C5, which is spectrally somewhat redder than the surrounding surface. (e) Telescopic CCD image of the dome field around Arago. (f) Clementine UV-vis ratio image of the region around Arago. Scale bars indicate the average pixel scale of each image (cf. Section 3.2).

towards high-TiO<sub>2</sub> lavas. The volumes of different basalt types seem to be rather similar, in contrast to Mare Fecunditatis, where low-TiO<sub>2</sub> lavas constitute most of the mare basalts and high-TiO<sub>2</sub> lavas form only thin localized patches (Rajmon and

Spudis, 2001). According to Staid et al. (1996), the youngest basalt unit extends from the northwestern part of Mare Tranquillitatis around the western part of Lamont to the Apollo 11 landing site and is interpreted to contain the highest abundance

of TiO<sub>2</sub>. It comprises the complete dome field near Arago. A more extensive basalt unit covering the north, south, central, and eastern parts of Mare Tranquillitatis contains the mare domes near Cauchy and in northern Mare Tranquillitatis. Small redder patches between the strongly blue units have a lower but still relatively high TiO<sub>2</sub> content. As we will see later on, several domes of the Cauchy field and in northern Mare Tranquillitatis are associated with this basalt unit. The spectrally reddest unit with the lowest TiO<sub>2</sub> content covers the north-eastern and south-eastern corner of Mare Tranquillitatis and is presumably older than the high-TiO<sub>2</sub> basalts. It does not comprise any of the mare domes regarded in this study.

The other two dome fields examined in this study are situated in eastern Oceanus Procellarum, in a region also known as Mare Insularum near the craters Hortensius, Milichius, and Tobias Mayer (Fig. 3). They comprise the dome suite near Hortensius, the classical hemispherical dome Milichius  $\pi$ , and the cluster of domes and swells between Milichius and Tobias Mayer. These dome fields have been studied in some detail by Head and Gifford (1980), showing that domes of different shapes and slopes occur together. Low and flat domes, steep domes, cones, lava flows, and also sinuous rilles can be found in this region, suggesting various stages in the development of dome structures and different effusion rates.

The basalts of Oceanus Procellarum exhibit a wide range of spectral characteristics and ages (Hiesinger et al., 2003). According to Spudis (1993), Mare Insularum lies inside an ancient, strongly degraded multi-ring impact basin. The two dome fields cover an extensive part of northern Mare Insularum south of the outer rim of the Imbrium basin. Although these domes share some characteristics, they display significant differences which indicate variations in eruption style. Spectrally, large parts of Mare Insularum are influenced by basalt lavas of low to moderate TiO<sub>2</sub> content on which ejecta of the craters Copernicus, Kepler, and Eratosthenes are superimposed (Hiesinger et al., 2003). The geologic map by Wilhelms and McCauley (1971) shows that most basalts of this region are Imbrian mare materials with some units showing characteristics of Eratosthenian mare (Em) material.

The Hortensius domes have been described to be of Eratosthenian age due to apparent superposition on Imbrian mare material, but possibly contemporaneous with uppermost mare material (Wilhelms and McCauley, 1971), while some domes in the Milichius region are classified as Eratosthenian mare dome material (Emd) and included as part of an Em unit. The Em unit is described as a probably relatively thin cover of younger lava flows or pyroclastic materials over thicker accumulations of Imbrian mare material (Wilhelms and McCauley, 1971; Wenker, 1999).

### 3. Observations

#### 3.1. Spacecraft observations of lunar mare domes

Most lunar mare domes can only be observed under oblique illumination due to the shallow slopes of their flanks. Consequently, the Lunar Orbiter images mostly acquired at solar alti-

tudes between 20° and 30° display steeper effusive mare domes like, e.g., the Hortensius dome field, some (but not all) of the domes near Milichius (Fig. 4), the Marius Hills, and the Rümker complex. The shallower domes in Mare Tranquillitatis, however, are invisible in the Lunar Orbiter images. What is more, these images are not suitable for photogrammetric analysis aiming at generating topographic data due to the lack of geometric and photometric calibration; the relation between incident flux and pixel greyvalue is non-linear and unknown because the images were acquired on photographic film scanned on board the spacecraft.

While the Apollo images used for computing the lunar topographic orthophotomaps are virtually distortion-free, they cannot be used for photoclinometric analysis, again due to an unknown non-linear relation between incident flux and film density, and most of them were acquired at high solar altitude. As previously described, the morphometric properties of a limited number of volcanic edifices have been derived from the lunar topographic orthophotomaps by Pike and Clow (1981).

The fact that nearly all Clementine images were acquired at local lunar noon implies high illumination angles for the equatorial regions of the Moon, where the mare domes are situated. Consequently, these images are neither suitable for stereophotogrammetry nor photoclinometry or shape from shading. In this study, however, we will make use of Clementine UV–vis multi-spectral imagery to examine the spectral properties of lunar mare domes (cf. Section 5.2.1 for further details).

#### 3.2. Telescopic CCD imagery

Due to the lack of photometrically calibrated spacecraft imagery acquired under oblique illumination (cf. Section 3.1) we will utilize telescopic CCD images for the determination of the morphometric properties of lunar domes. We used telescopes with apertures between 125 and 400 mm in combination with digital CCD video cameras of different types (cf. Table 1). The Lumenera camera is a CCD camera for industrial purposes. Its image size amounts to 640 × 480 pixels, the size of the quadratic pixels to 7.4  $\mu$ m. The Atik and Philips ToUCam Pro webcams have the same image size of 640 × 480 pixels and a pixel size of 5.6  $\mu$ m. We generated each image by stacking several hundreds of video frames. For this purpose we made use of the Registax and Giotto software packages, employing a cross-correlation technique similar to the one described by Baumgardner et al. (2000). In that work, however, digitized analog video tapes were processed, while we directly acquired digital video frames. The scale of our images is between 250 and 600 m per pixel on the lunar surface. Due to atmospheric seeing, however, the effective resolution (denoted by the diameter of the point spread function rather than the spatial resolution per pixel) of our best images approximately corresponds to 1 km on the lunar surface. The images shown in Figs. 2b and 3e were taken in the Johnson I band, a bandpass filter transmitting near-infrared wavelengths between 700 and 1100 nm, while the other telescopic images were acquired in integral visible light through a UV + IR block filter which transmits wavelengths between 400 and 700 nm.

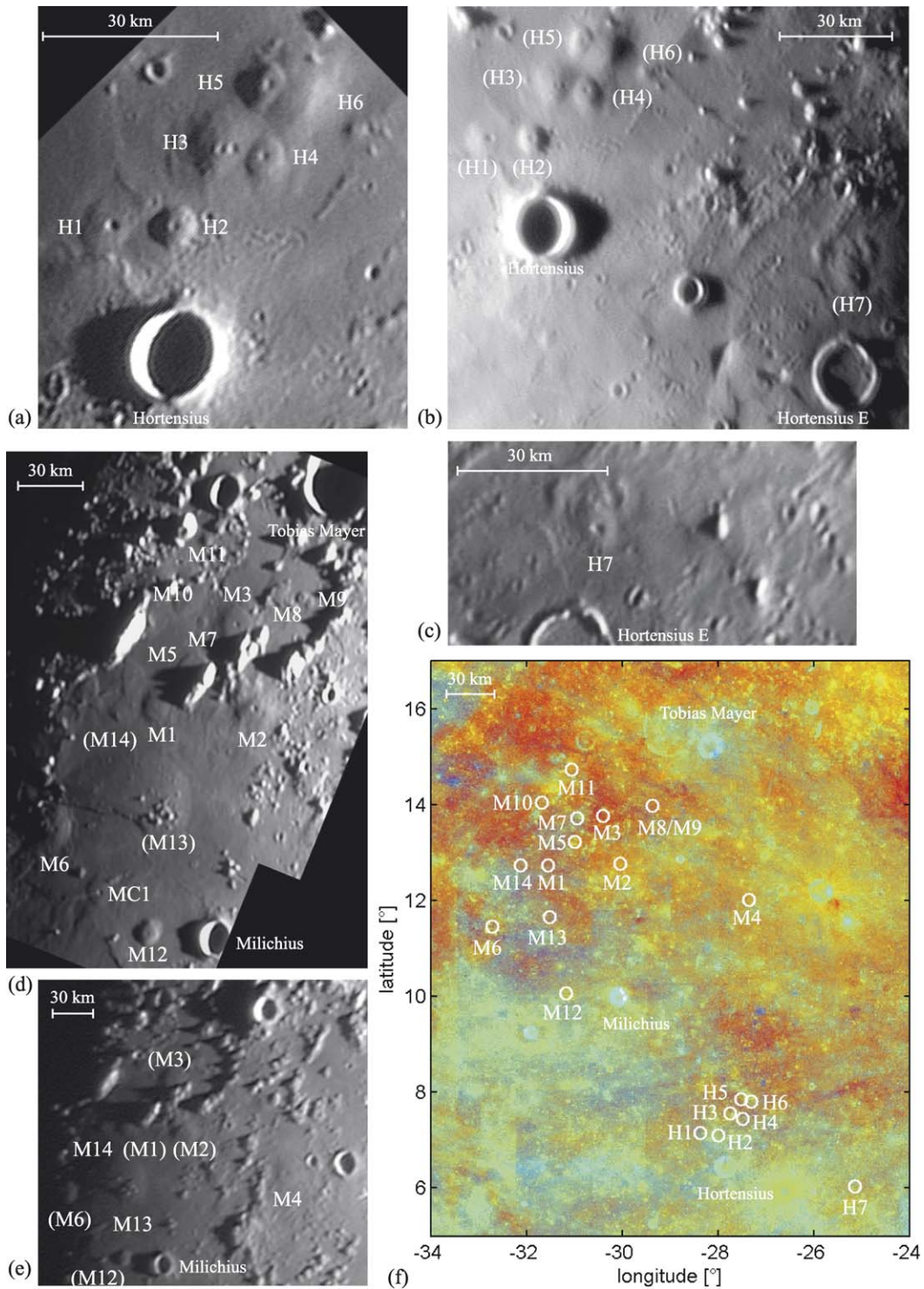


Fig. 3. (a) Telescopic CCD image of the dome field north of Hortensius. (b) Telescopic CCD image of the region between Hortensius and Hortensius E. (c) Telescopic CCD image of dome H7 north of Hortensius E. (d) Telescopic CCD image of the dome field between Tobias Mayer and Milichius. (e) Lower-resolution telescopic CCD image, showing dome M4 which is not apparent in (d). (f) Clementine UV-vis ratio image, indicating the locations of the examined domes. Scale bars indicate the average pixel scale of each image (cf. Section 3.2).

In Figs. 2 and 3 the domes analyzed in this study are indicated. The telescopic CCD images in the figures are not geometrically rectified, which implies a non-uniform direction-dependent pixel scale. The scale bars in Figs. 2 and 3 therefore indicate the average pixel scale for each image. Labels without

brackets denote that a 3D reconstruction of the corresponding dome has been performed based on the respective image, while labels in brackets are merely shown for comparison. For our set of lunar domes, the image sections used for 3D reconstruction were extracted from the telescopic CCD images shown in

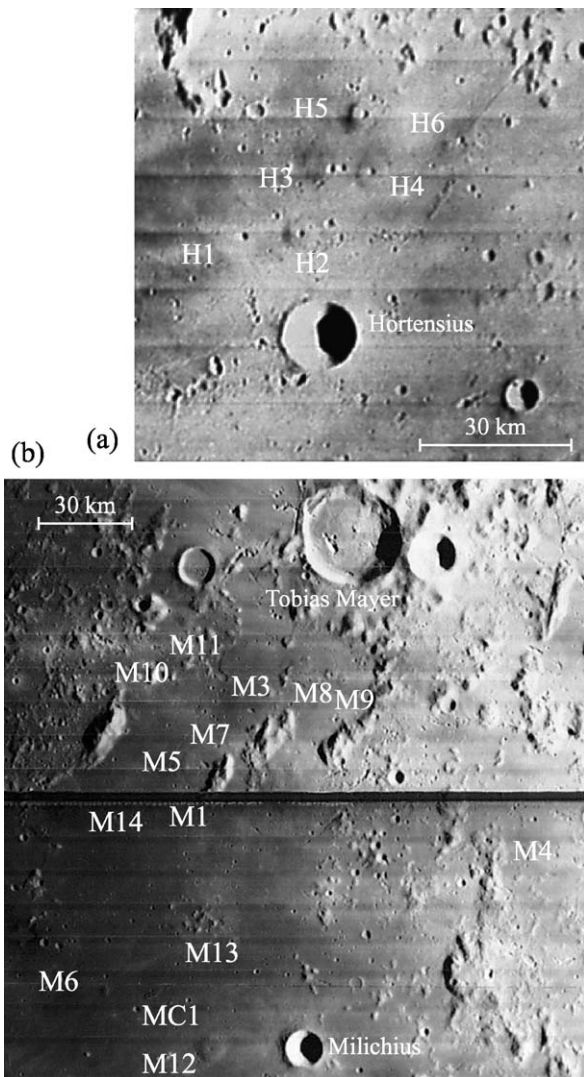


Fig. 4. (a) Dome field north of Hortensius (Lunar Orbiter image IV-133-H1). (b) Dome field between Milichius and Tobias Mayer (Lunar Orbiter image IV-133-H2). Not all domes are well visible in this image. Note that the images in (a) and (b) are of different scale.

Figs. 2 and 3 and are shown in Fig. 5 at uniform scale. North is to the top and west to the left, and the image sections have been rectified to simple cylindrical projection.

Image-based 3D reconstruction approaches like those described in Sections 4.2 and 4.3 assume that the greyvalue  $I$  of a pixel is proportional to the incident flux  $F$ . Especially for webcams this is not necessarily the case because it is often possible to adjust the gamma value  $\gamma$  manually from within the camera control software, causing the greyvalue  $I$  to be proportional to  $F^\gamma$ . The Lumenera industrial CCD camera was set to linear hardware mode with  $\gamma = 1$ . The Atik and the Philips ToUCam Pro CCD cameras, equipped with Sony CCD sensors of similar type, have no hardware-specified linear mode, such that they were utilized at different gamma settings. Hence, we performed a calibration of the gamma scale in the camera control software by evaluating flatfield frames of different intensities acquired through different neutral density filters with known transmission coefficients, then fitting a characteristic curve of the form  $I = aF^\gamma$  to the measured flatfield intensities. From this calibration procedure we obtained  $\gamma = 1.0$  for the images acquired with the Atik camera (Figs. 3a and 3d) and  $\gamma = 0.93, 0.85, 0.93,$  and  $0.94$ , respectively, for the images acquired with the Philips ToUCam (Figs. 2b, 3b, 3c, and 3e).

#### 4. Image-based determination of 3D morphometric data

In this section we will describe how the three-dimensional shape of a lunar dome and its morphometric parameters (diameter, height, flank slope, edifice volume) are determined based on the analysis of the shadow cast by the dome and the photometric evaluation of the correspondingly calibrated image pixel intensities.

##### 4.1. Shadow analysis

By far the oldest method for estimating altitudes (or better: altitude differences) on the lunar surface is the analysis of shadow lengths. In our CCD images we measured the diameter  $D$  of the dome and the length  $l$  of its shadow in pixels. The corresponding image scale in kilometers per pixel was obtained by

Table 1  
List of telescopic CCD observations performed for this study

Figure	UT date and time	Telescope	Camera	Filter
2a	13 Apr 2005, 19:34	250 mm reflector	Lumenera LU075	UV + IR block
2b	15 Mar 2005, 20:14	200 mm reflector	Philips ToUCam	Johnson I
2e	01 Jan 2005, 01:49	250 mm reflector	Lumenera LU075	UV + IR block
3a	19 Feb 2005, 02:28	400 mm reflector	Atik BW	UV + IR block
3b	03 Apr 2005, 19:24	310 mm reflector	Philips ToUCam	UV + IR block
3c	16 Jul 2005, 08:41	310 mm reflector	Philips ToUCam	UV + IR block
3d	22 Dec 2004, 02:37	200 mm refractor	Atik BW	UV + IR block
3e	23 Oct 2004, 19:25	200 mm reflector	Philips ToUCam	Johnson I
12a	19 May 2005, 20:42	200 mm reflector	Philips ToUCam	Johnson I
12b	29 Dec 2004, 00:55	250 mm reflector	Philips ToUCam	UV + IR block
12c	26 Feb 2005, 09:28	200 mm refractor	Atik BW	UV + IR block
12d	12 Jan 2003, 17:19	125 mm reflector	Philips ToUCam	–
12e	12 Aug 2004, 03:21	200 mm reflector	Philips ToUCam	Johnson I
12f	16 Oct 2004, 21:02	250 mm reflector	Philips ToUCam	UV + IR block

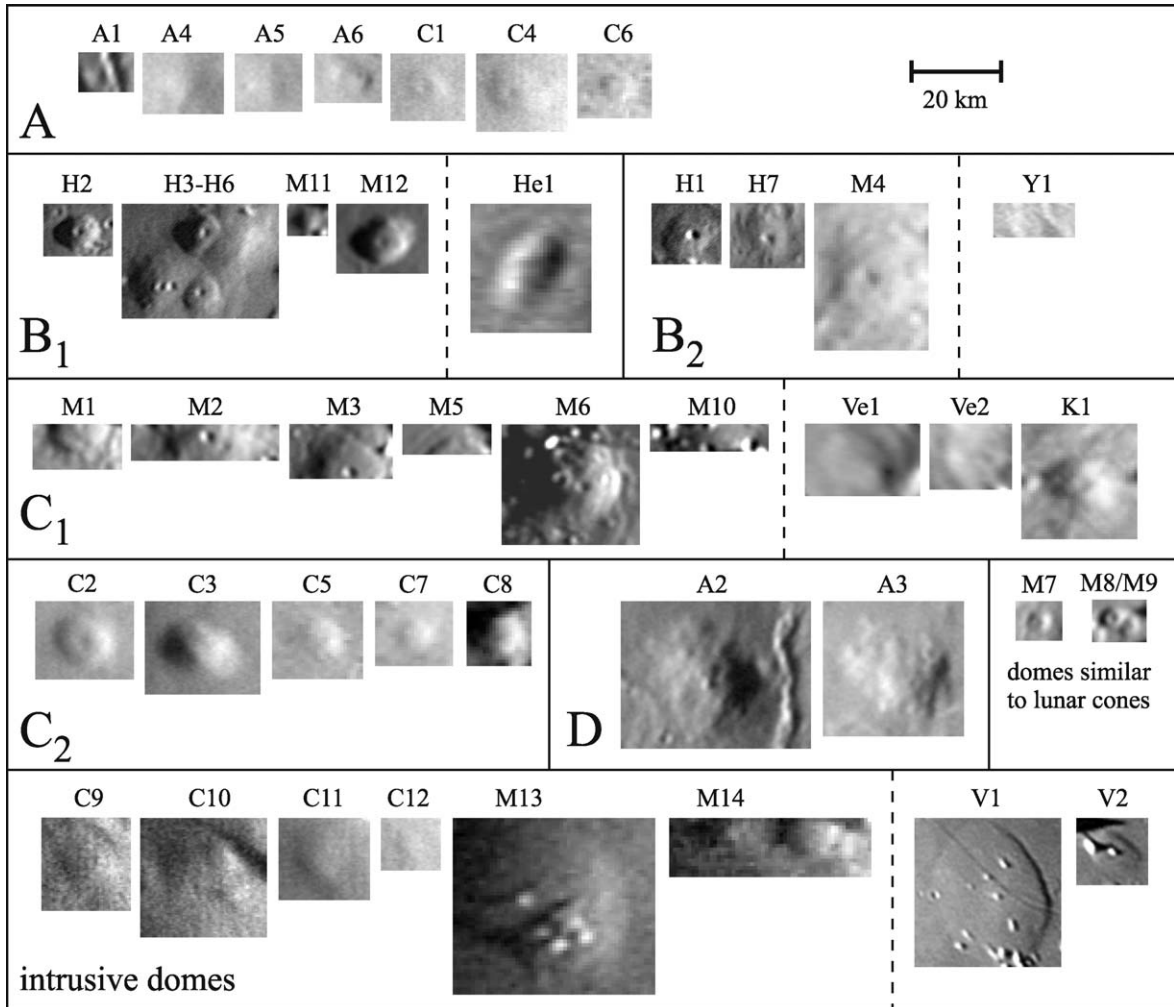


Fig. 5. The domes of our data set, all displayed at the same scale and arranged according to the classes determined in Section 5.3. These regions of interest have been used for 3D reconstruction according to Section 4.2 and 4.3.

measuring the diameters of craters of known size in the field of view. From the shadow length  $l$ , corrected for foreshortening, and the local solar altitude  $\mu$  the height  $h$  of the dome is given by

$$h = l \tan \mu. \quad (1)$$

The possible effect of sloping terrain has to be carefully considered, as the measured shadow length will be longer for downward slope and shorter for upward slope, compared to horizontal terrain. A further problem arising especially for shallow domes is that even under highly oblique illumination the shadow does not begin at the dome summit but at some point on its flank, such that the value of  $h$  computed according to Eq. (1) merely represents a lower limit to the true dome height.

Ashbrook (1961) has shown that the average slope of the dome flank equals the solar altitude when the shadow covers one quarter of the dome diameter, assuming a hemispherical shape of the dome. The observer determines the moment in time, corresponding to a solar altitude  $\tilde{\mu}$ , for which  $l = D/4$  is given, leading to a dome height  $h = (D/2) \tan \tilde{\mu}$ . The Ashbrook method has primarily been devised for visual observations. The assumption of hemispherical dome shape, however, represents

Table 2

Dome slope and height values determined using the shadow-based method by Ashbrook (1961)

Dome	Slope [°]	Height [m]
C11	0.6	60
A2	1.5	310
H7	1.5	100
M11	3.0	150
M12	2.7	230

a significant restriction to its applicability. In this study, we used it to determine the heights of domes C11, A2, H7, M11, and M12 (cf. Table 2), yielding slope and height values consistent with those obtained by the image-based 3D reconstruction approaches described in Sections 4.2 and 4.3.

#### 4.2. Photoclinometry

Photoclinometric and shape from shading techniques take into account the geometric configuration of camera, light source, and the object itself, as well as the reflectance properties of the surface to be reconstructed. For parallel incident

light and an infinite distance between camera and object the intensity  $I(u, v)$  of image pixel  $(u, v)$  amounts to

$$I(u, v) = R(\rho, \vec{n}, \vec{s}, \vec{v}). \quad (2)$$

Here,  $\rho$  is the surface albedo,  $\vec{n}$  the surface normal,  $\vec{v}$  the direction to the camera,  $\vec{s}$  the direction of incident light, and  $R$  the reflectance function. A well-known example is the Lambertian reflectance function  $R(\rho, \vec{n}, \vec{s}) = \rho \cos \theta_i$ , where  $\theta_i$  denotes the incidence angle between  $\vec{n}$  and  $\vec{s}$  with  $\cos \theta_i = \vec{n} \cdot \vec{s} / (|\vec{n}| |\vec{s}|)$ . The surface is described by the function  $z(x, y)$ ; in practice, however, it turns out to be advantageous to utilize the formulation  $z(u, v)$  defined at the discrete pixel positions  $(u, v)$ .

In the following, the surface normal  $\vec{n}$  is represented in gradient space by the directional derivatives  $p = \partial z / \partial x$  and  $q = \partial z / \partial y$  of the surface function  $z(x, y)$  with  $\vec{n} = (-p, -q, 1)$ . In an analogous manner we define  $\vec{s} = (-p_s, -q_s, 1)$  and  $\vec{v} = (-p_v, -q_v, 1)$ . In the following we assume an infinite distance between the surface, the light source (the Sun), and the camera, respectively. Accordingly, the reflectance function  $R$  can be expressed in terms of the surface gradients  $p(u, v)$  and  $q(u, v)$  at each pixel position and the constant vectors  $\vec{s}$  and  $\vec{v}$ , leading to the formulation  $I(u, v) = R(\rho(u, v), p(u, v), q(u, v), \vec{s}, \vec{v})$ .

The Lambert model does not correspond very well to the true reflectance behavior of the lunar surface. A much more appropriate relation is the physically motivated photometric model by Hapke (1993) which is based on the theory of radiative transfer. It allows conclusions about certain surface properties such as the average particle size, the particle density, the albedo of the surface material, and the macroscopic surface roughness. Sets of Hapke parameters valid for the lunar regolith are given, e.g., by Warell (2004). It is not straightforward, however, to directly employ the Hapke model for 3D reconstruction purposes. Therefore, in many astrogeological applications the comparably simple, empirical lunar-Lambert law,

$$R(\rho, \theta_i, \theta_e, \alpha) = \rho \left[ 2L(\alpha) \frac{\cos \theta_i}{\cos \theta_i + \cos \theta_e} + (1 - L(\alpha)) \cos \theta_i \right], \quad (3)$$

is used (McEwen, 1991). In Eq. (3),  $\theta_e$  denotes the emission angle between the surface normal  $\vec{n}$  and the viewing direction  $\vec{v}$  with  $\cos \theta_e = \vec{n} \cdot \vec{v} / (|\vec{n}| |\vec{v}|)$ . The lunar-Lambert parameter  $L(\alpha)$  is an empirical value depending on the phase angle  $\alpha$  between  $\vec{s}$  and  $\vec{v}$ . The lunar-Lambert model is a weighted sum of the Lommel–Seeliger law and the Lambert law. Given a suitable choice of  $L(\alpha)$ , it fits the true reflectance behavior of many planetary surfaces equally well as the Hapke model. Values for  $L(\alpha)$  have been tabulated by McEwen (1991) for planetary surfaces with a wide range of regolith properties. McEwen (1991) demonstrates that for low-albedo surfaces like that of the Moon,  $L(\alpha)$  is mainly governed by Hapke's macroscopic surface roughness parameter  $\bar{\theta}$  (Hapke, 1993). According to recent work on lunar photometric modeling by Warell (2004), we assume  $\bar{\theta} = 11^\circ$ .

We will make use of a single-image approach to 3D surface reconstruction which is applicable to smooth, untextured surface parts without absolute radiometric calibration. According to Eq. (2), we attempt to determine two variables  $p(u, v)$

and  $q(u, v)$  for each pixel from one single measurement, the pixel intensity  $I(u, v)$ . In a first step we therefore follow a photoclinometric approach, which consists of computing height profiles along image rows. For all domes in our data set, the terrain is gently sloping ( $|p|, |q| \ll 1$ ), the illumination is highly oblique, and the scene is illuminated nearly exactly from the east or the west, corresponding to  $q_s = 0$ . The lunar-Lambert reflectance (3) thus depends much stronger on  $p$  than on  $q$ , such that we may set  $q = 0$ . Note that this approximation is exact for cross-sections in east–west direction through the summit of a feature, while it is otherwise a reasonable approximation. An early description of the principle of photoclinometry is given by Wilhelm (1964).

We assume a constant albedo  $\rho$ , which is justified for all examined domes as they are virtually undistinguishable from their surroundings in Clementine 750 nm images. The value of  $\rho$  is chosen such that the average surface slope over the region of interest is zero. Under these assumptions, Eq. (2) is solved for the surface gradient  $p(u, v)$  for each pixel with intensity  $I(u, v)$ . With Eq. (3) representing the reflectance function, an analytical solution of Eq. (2) does not exist, such that we utilize Newton's method (Press et al., 1992): The root  $r$  of a function  $f(x)$  with  $f(r) = 0$  is obtained iteratively, starting with an initial value  $x_0$  and then following the update rule  $x_{n+1} = x_n - f(x_n)/f'(x_n)$ . As long as  $x_0$  is chosen not too far from the root  $r$ ,  $x_n$  will converge towards  $r$  already after a small number  $n$  of iterations. For each image row  $v$ , a height profile  $z(u, v)$  can then be obtained by integration of the surface gradients  $p(u, v)$ .

### 4.3. Shape from shading

The result of photoclinometry is refined in a second step by means of a more sophisticated, variational approach described in detail by Horn (1989). It primarily consists of minimizing the sum of squared differences between the observed pixel intensities  $I(u, v)$  and the modeled reflectances  $R(\rho(u, v), p(u, v), q(u, v))$ .

Our ground-based images are affected by a slight blur due to atmospheric seeing. Hence, the observed image  $I(u, v)$  is assumed to be a convolution  $G * I_0(u, v)$  of the true image  $I_0(u, v)$  with a Gaussian point spread function (PSF)  $G$ . The half width  $\sigma$  of the Gaussian PSF  $G$  is determined from the intensity profile of shadows cast by steep mountains, e.g., crater rims, where an abrupt transition from illuminated surface to darkness is expected. Convoluting a synthetically generated abrupt change in intensity with a Gaussian PSF and comparing the result with the intensity profile observed in the image allows for an estimation of the PSF half width  $\sigma$ . A similar method is used by Baumgardner et al. (2000) to estimate the PSF for ground-based Mercury images, using the limb of the planetary disk as a reference. The intensity error term is then given by

$$e_i = \sum_{u,v} \left[ I(u, v) - G * R(\rho, p(u, v), q(u, v)) \right]^2 \quad (4)$$

(Joshi and Chaudhuri, 2004). The uniform surface albedo  $\rho$  and approximate values for the surface gradients  $p(u, v)$  in east–west direction are known from Section 4.2, obtained there under

the assumption of zero values of the surface gradients  $q(u, v)$  in north–south direction. Horn (1989) emphasizes that  $p(u, v)$  and  $q(u, v)$  are not independent of each other but represent directional derivatives of the same surface  $z(u, v)$ . In other words, they have to form an integrable vector field. As a consequence,  $z(u, v)$  has to be chosen such that the departure from integrability error term,

$$e_s = \sum_{u,v} \left[ \left( \frac{\partial z}{\partial x} - p \right)^2 + \left( \frac{\partial z}{\partial y} - q \right)^2 \right], \quad (5)$$

is minimized simultaneously with  $e_i$ . We therefore have to minimize the overall error term  $e = e_i + \lambda e_s$ , where the Lagrange parameter  $\lambda$  denotes the relative weight of the error terms. For this purpose we utilize the iterative scheme by Horn (1989), which simultaneously adjusts  $p(u, v)$ ,  $q(u, v)$ , and  $z(u, v)$ . The iteration is initialized with the  $p(u, v)$  values obtained in Section 4.2 and with  $q(u, v) = 0$ . In the course of the iteration process,  $p(u, v)$  hardly changes, and  $q(u, v)$  obtains values consistent with the integrability error term (5).

Typical 3D reconstruction results obtained with this algorithm are shown in Fig. 6, illustrating the rich variety of 3D shapes occurring in the examined four lunar dome fields. For example, dome C1 near Cauchy is remarkably shallow but clearly effusive due to its central crater pit. The nearby domes C2 and C3, traditionally known as Cauchy  $\omega$  and  $\tau$ , are steeper but quite different in shape, since C2 clearly displays a flattened top with a summit crater pit while C3 is of more conical shape. The large edifices A2 and A3, traditionally designated Arago  $\alpha$  and  $\beta$ , are somewhat irregularly shaped, while dome A1 next to A2, situated near a mare ridge, is of regular conical shape. The domes near Hortensius have large and deep summit crater pits. This is true even for the comparably shallow dome H7 displaying a summit crater pit with a depth corresponding to about at least half the height of the dome. The domes near Milichius show remarkably manifold 3D shapes. Examples are M3 with its pancake-like shape, M4 and M6 with their rougher and more strongly textured surfaces, and M12 showing a very regular, flattened shape which is quite similar to that of C2, with a central summit crater pit.

#### 4.4. Features derived from 3D reconstruction

The image scale (in kilometers per pixel) was obtained for each image relying on craters of known diameters. The dome diameter  $D$  was measured in pixels; for non-circular domes an appropriate average value was used. The height  $h$  of a dome was obtained by measuring the altitude difference in the reconstructed 3D profile between the dome summit and the surrounding surface, taking into account the curvature of the lunar surface. The average flank slope  $\zeta$  was determined according to

$$\zeta = \arctan \frac{2h}{D}. \quad (6)$$

The dome volume  $V$  was computed by integrating the reconstructed 3D profile over an area corresponding to a circular region of diameter  $D$  around the dome center. If only a part of the dome could be reconstructed, as it was the case for a few

domes in the Milichius field due to shadows cast on the dome surfaces by nearby hills, the volume was estimated based on a cross-section through the center of the dome, assuming rotational symmetry. A rough quantitative measure for the shape of the dome is given by the form factor

$$f = \frac{V}{\pi h(D/2)^2}. \quad (7)$$

We have  $f = 1/3$  for domes of conical shape,  $f = 1/2$  for parabolic shape,  $f = 1$  for cylindrical shape, and intermediate values for hemispherical shape. For effusive domes, it was possible in some cases to measure the diameter  $D_c$  of the summit crater pit in the telescopic images. The reconstructed 3D profiles also yield values for the depth  $d_c$  of the crater pit, but due to insufficient resolution, the obtained values must be regarded as lower limits to the true depth rather than accurate measurements. For the domes H3 and M6 having two crater pits, respectively, only the larger crater is considered in the subsequent analysis.

The spectral properties derived from Clementine UV–vis data and the morphometric quantities derived from the telescopic CCD images and reconstructed 3D profiles of the lunar domes examined in this study are listed in Table 3, respectively. If possible, we identify the examined domes with the preliminary names assigned by Head and Gifford (1980), consisting of the name of the nearest crater and a number, as well as traditional, mostly unofficial designations for some of the well-known domes. A more comprehensive catalogue of lunar domes has recently been published by Kapral and Garfinkle (Kapral, C., Garfinkle, R., 2005, GLR Lunar Dome Catalog. <http://www.glrgroup.org/domes/kapralcatalog.htm>): The quantities listed in Table 3 will be used in Section 5 for further analysis and to establish a classification scheme based on morphometric quantities, and in Section 6 to discuss the geologic mechanisms that may be responsible for the observed spectral and morphometric properties of lunar mare domes.

#### 4.5. Error estimation

In the context of image-based 3D reconstruction of the domical structure, three main sources of error can be found. The parameter  $L(\alpha)$  of the reflectance function is not exactly known and may show variations over the surface for different terrain types. We assume a standard error of  $L(\alpha)$  of  $\pm 0.15$ , an error range that also includes larger values of the macroscopic surface roughness  $\bar{\theta}$  of up to  $20^\circ$  (McEwen, 1991, Fig. 16 therein). The half width  $\sigma$  of the Gaussian PSF for our telescopic CCD images could be estimated at an accuracy of about  $\pm 0.5$  pixels. We have found that the uncertainties in  $L(\alpha)$  and  $\sigma$  affect the measured height values of the lunar domes by no more than a few meters and can therefore be regarded as irrelevant. We expect the influence of the PSF to become more important for strongly wrinkled surfaces.

A more important issue is the slight non-linearity of the CCD sensor, which is compensated by the gamma calibration procedure described in Section 3.2. The uncertainty of the determined gamma values approximately amounts to  $\pm 0.05$  for

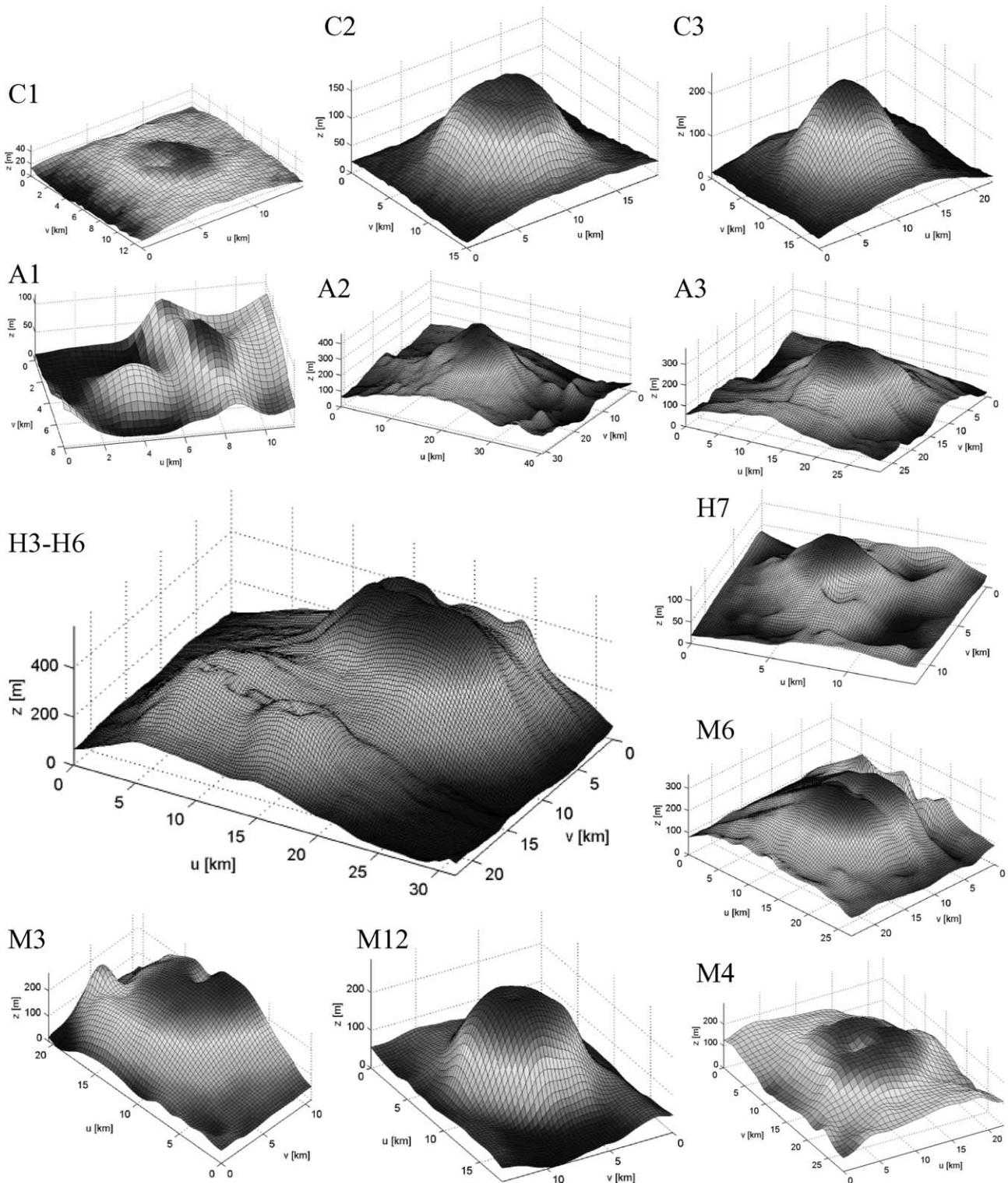


Fig. 6. Typical 3D reconstruction results for the examined four fields of lunar mare domes. The dome identification according to Table 3 is indicated on the upper left of each plot, respectively. For C1, C2, and C3, the  $z$  axis is exaggerated by a factor of 50, for the other domes by a factor of 30.

the Atik and the ToUCam CCD cameras. The Lumenera CCD camera has a linear ( $\gamma = 1.0$ ) characteristic curve.

The uncertainty in  $\gamma$  results in a relative standard error of the dome height  $h$  of 10%, which is independent of the height value itself. The dome diameter  $D$  can be measured at an accuracy of 5%, since the outer rim is not well-defined for most domes.

Based on experiments, we found that these uncertainties in  $h$  and  $D$  lead to a typical standard error of the edifice volume  $V$ , computed by integration of the 3D profile, of about 20%.

Furthermore, we have examined possible systematic deviations between the true values for dome height and volume and the results obtained with the described photogrammetry

Table 3  
Spectral and morphometric properties of the lunar domes examined in this study

Dome	Long. [°]	Lat. [°]	$R_{750}$	$R_{415}/R_{750}$	$R_{950}/R_{750}$	$\zeta$ [°]	$D$ [km]	$h$ [m]	$V$ [km <sup>3</sup> ]	$f$	$D_c$ [km]	$d_c$ [m]	Name
Effusive mare domes													
C1	37.48	7.11	0.086310	0.650797	1.058752	0.35	8.1	25	0.65	0.50	2.6	>15	Cauchy 5
C2	38.32	7.23	0.090923	0.637728	1.056679	1.17	12.2	125	7.4	0.50	2.6	>20	Cauchy 1 (Cauchy $\omega$ )
C3	36.73	7.58	0.091906	0.631818	1.060832	1.28	17.0	190	12	0.30			Cauchy 2 (Cauchy $\tau$ )
C4	36.78	8.85	0.081955	0.662070	1.054672	0.43	13.3	50	3.2	0.46	2.2	>10	
C5	33.02	10.56	0.090238	0.645200	1.048875	1.03	11.1	100	5.4	0.56			
C6	31.97	10.76	0.084180	0.655800	1.068522	0.74	7.7	50	0.99	0.43			
C7	35.86	14.18	0.095748	0.619000	1.043627	1.48	8.5	110	3.8	0.61			Grace
C8	30.72	14.40	0.097474	0.634600	1.046517	2.5	12.5	270	17	0.51			
A1	21.96	7.66	0.086290	0.670275	1.057695	0.88	5.6	45	0.32	0.29			
A2	21.7	7.56	0.088621	0.662097	1.056488	1.5	25.4	330	67	0.40			Arago 2 (Arago $\alpha$ )
A3	20.07	6.24	0.091150	0.673800	1.057823	1.3	23.6	270	39.9	0.34			Arago 1 (Arago $\beta$ )
A4	21.27	8.65	0.080645	0.668067	1.076219	0.66	11.1	65	3.2	0.50			Arago 3
A5	20.96	8.88	0.081562	0.671936	1.073064	0.59	8.4	45	1.4	0.58			Arago 4
A6	20.79	9.22	0.080504	0.679090	1.075120	0.58	9.5	50	1.8	0.50			Arago 5
H1	-28.41	7.18	0.130829	0.620300	1.027800	1.89	8.48	140	3.4	0.44	2.6	>95	Hortensius 1
H2	-28.01	7.12	0.128088	0.622500	1.013100	3.45	7.63	230	6.3	0.60	1.9	>45	Hortensius 2
H3	-27.78	7.59	0.117386	0.610500	1.019700	2.05	12.3	220	17	0.65	1.7	>65	Hortensius 3
H4	-27.51	7.47	0.120880	0.615400	1.030300	3.21	6.78	190	5	0.73	1.9	>40	Hortensius 4 (Hortensius $\sigma$ )
H5	-27.54	7.87	0.118260	0.606600	1.028700	5.39	8.48	400	18	0.81	1.6	>50	Hortensius 5
H6	-27.34	7.82	0.123721	0.611800	1.021300	3.57	12.5	390	32	0.66			Hortensius 6
H7	-25.17	6.07	0.146308	0.614929	1.015627	1.47	7.82	100	2.4	0.51	2.4	>45	
M1	-31.58	12.76	0.109029	0.605980	1.044387	0.86	13.4	100	8.2	0.58	2.4		Tobias Mayer 1
M2	-30.05	12.79	0.126708	0.583711	1.028431	1.8	20.1	320	50	0.49	3.7	>60	Tobias Mayer 4
M3	-30.43	13.78	0.106287	0.592251	1.053758	1.4	15.6	190	12	0.34	3.1	>70	Tobias Mayer 3
M4	-27.39	12.04	0.138348	0.598031	1.024634	1.27	15.3	170	21	0.69	4.0	>35	Tobias Mayer 6
M5	-31.01	13.24	0.118107	0.597823	1.018403	0.6	15.3	80	6.8	0.46			Tobias Mayer 2
M6	-32.74	11.48	0.102415	0.606829	1.027200	1.34	19.7	230	33	0.47	3.0	>70	
M7	-30.96	13.75	0.116819	0.615113	1.023343	0.99	5.2	45	0.37	0.39	1.8		
M8	-29.4	14.00	0.121432	0.595118	1.042788	3.46	4.3	130	1.2	0.65	1.8		
M9	-29.4	14.00	0.121432	0.595118	1.042788	3.15	4.0	110	0.88	0.64	0.9		
M10	-31.7	14.06	0.122697	0.597564	1.032913	0.84	19.0	140	21	0.54	3.4	>35	Tobias Mayer 7
M11	-31.08	14.77	0.118580	0.590804	1.029727	2.8	6.0	150	2.3	0.54	2.4		
M12	-31.2	10.08	0.115645	0.611552	1.011650	2.72	9.7	230	11	0.63			Milichius 1 (Milichius $\pi$ )
Intrusive domes													
C9	34.66	7.06	0.085953	0.650281	1.065746	0.13	13.3	15	0.47	0.23			
C10	35.19	10.00	0.090151	0.641432	1.058241	0.3	19.2	50	10	0.72			
C11	36.75	11.06	0.085275	0.665611	1.056640	0.7	12.2	75	6.4	0.73			
C12	37.2	12.37	0.090441	0.616503	1.068145	0.45	6.3	25	0.48	0.61			
M13	-31.53	11.68	0.102386	0.611853	1.037711	0.41	27.8	100	15	0.25			
M14	-32.13	12.76	0.105568	0.609384	1.037413	0.27	14.8	35	1.7	0.28			
Highland domes (for comparison)													
G1	-40.38	36.43	0.171989	0.564804	1.067882	8.3	19.0	1320	187	0.5			Gruihuisen $\gamma$
G2	-39.42	36.11	0.155208	0.550575	1.058267	6.9	27.0	1630	378	0.5			Gruihuisen $\delta$
G3	-40.86	36.92	0.149193	0.560447	1.064689	9.1	7.5	1020	23	0.5			Northwest dome
Effusive mare domes in other lunar regions (for comparison)													
Y1	49.96	14.82	0.158761	0.591163	1.065435	1.31	9.6	110	4.8	0.60			
Ve1	57.83	-15.74	0.140983	0.591312	1.062839	0.55	16.8	80	7.2	0.41			
Ve2	59.00	-17.75	0.158890	0.603765	1.056680	0.25	13.5	30	2.1	0.50	3.0	>7	
K1	-24.18	-26.84	0.116926	0.629810	1.046385	1.35	13.6	160	13	0.55	3.5	>30	Kies 1 (Kies $\pi$ )
He1	-50.00	20.21	0.108468	0.624548	0.975274	2.5	14.4	230	21	0.56			Aristarchus 1 (Herodotus $\omega$ )
Lunar cones (for comparison)													
SC1	27.6	18.6	0.088198	0.664551	1.036190	3.54	2.3	72	0.16	0.52			Osiris
SC2	27.5	18.9	0.087239	0.660910	1.038922	4.0	1.7	60	0.071	0.52			Isis
MC1	-31.7	10.7	0.097661	0.616680	1.042645	3.9	1.8	61	0.081	0.52			
Intrusive domes in other lunar regions (for comparison)													
V1	10.2	30.7	0.119482	0.596726	1.013374	0.55	30	130	42	0.46			Valentine
V2	10.26	31.89	0.111639	0.592124	1.034287	0.62	11	80	1.9	0.34			

For further details cf. Section 4.4.

and shape from shading method. No sufficiently accurate morphometric lunar dome properties are available as ground truth values, and our method cannot be directly applied to images of terrestrial volcanoes (for which such data are available) since it is usually not possible to describe the reflectance behavior of the terrestrial surface by a relatively simple relationship like the lunar-Lambert law. We therefore performed experiments on synthetic ground truth data, which is a common practice in the domain of computer vision (Wöhler and Hafezi, 2005). We regarded rendered images of a dome of parabolic shape with a diameter of 12 km and a height of 200 m, yielding an average flank slope of  $1.91^\circ$ , a form factor of 0.5 (Wilson and Head, 2003), and an edifice volume of  $11.31 \text{ km}^3$ . Image scale was set to 300 m per pixel. We assumed the synthetic dome to be located on the lunar equator at 10 different equally spaced selenographic longitudes  $\lambda_s$  between  $-45^\circ$  and  $+45^\circ$ . We rendered images of the dome under sunrise illumination at solar altitudes  $\mu$  of  $4^\circ$  and  $6^\circ$  for each value of  $\lambda_s$ . Assuming zero libration, the phase angle amounts to  $\alpha = 90^\circ + \lambda_s - \mu$ , and the lunar-Lambert parameter  $L(\alpha)$  was chosen according to McEwen (1991) for each rendered image. For all examined configurations of  $\lambda_s$  and  $\mu$ , the root mean square deviation between the reconstructed and the true 3D profile is smaller than 5 m. The deviations between the dome height and volume determined from the synthetic images based on our photoclinometry and shape from shading approach and the respective ground truth values are always smaller than 1%. Hence, we may conclude that our reconstruction results are not perceptibly affected by systematic errors.

The dome height values independently obtained in Section 4.1 based on shadow length measurement according to Ashbrook (1961) may also be used for comparison, yielding a good consistency with the corresponding values obtained by photoclinometry and shape from shading (cf. Table 2).

When no ground truth is available, the consistency of height measurements across several images is a further good indicator of their reliability. We have determined the height values of the domes M3 and M12 based on the images in Figs. 3d and 3e, which were acquired with different telescopes and CCD cameras from different locations. The obtained dome heights are 190 m and 230 m in Fig. 3d, compared to 170 and 210 m in Fig. 3e, respectively, which is a reasonable correspondence.

A further independent test of the reconstruction result in the absence of ground truth data, suggested by Horn (1989), is the comparison of a second image of the surface part acquired under illumination conditions strongly different from those valid for the image used for 3D reconstruction with a corresponding synthesized view of the surface, generated based on the reconstructed 3D profile. We have performed such a comparison for the domes H3–H6 and H7 (Fig. 7). The 3D reconstruction was based on Figs. 3a and 3c, respectively, which were both acquired at local sunrise, while Fig. 3b taken at local sunset is used for comparison. Fig. 7 reveals a good correspondence between details in the rendered images and their real counterparts, especially concerning the length of shadows, which are reliable indicators of elevation differences on the surface.

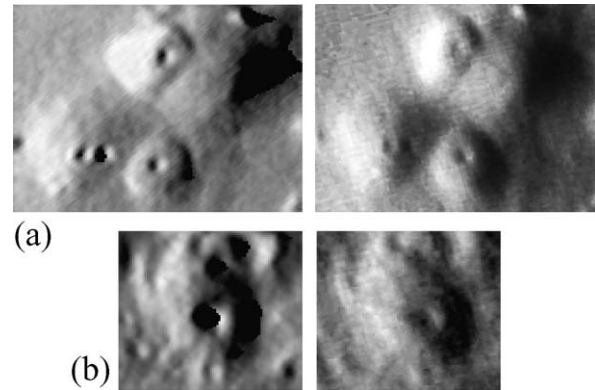


Fig. 7. Comparison between synthetic images (left column), rendered based on the reconstructed 3D profile, and real images acquired under illumination conditions strongly different from those valid for the images used for 3D reconstruction (right column). (a) Domes H3–H6 north of Hortensius. (b) Dome H7 north of Hortensius E.

#### 4.6. Comparison to previous height measurements

Not too much topographic data about lunar domes have been published yet. The most significant contribution to this field has been provided by Brungart (1964), who compiled a catalogue of 261 domes reporting their coordinates, diameters, heights, slopes, and morphological characteristics, utilizing the orthographic lunar atlas (Kuiper, 1961) that consists of telescopic photographs. Brungart (1964) determines values for the dome heights and flank slopes based on shadow length measurement but at the same time characterizes the obtained results as merely representing order of magnitude estimates. As an example, for Arago  $\alpha$  and  $\beta$  (entries no. 3 and 4 in the Brungart catalogue) a height of 700 and 800 m with an average slope of  $5.5^\circ$  and  $6.0^\circ$  is reported, respectively. Our results indicate lower heights of 330 and 270 m along with slopes of  $1.5^\circ$  and  $1.3^\circ$ , respectively. For Milichius  $\pi$  (entry no. 190), Brungart states a height of 742 m with an average slope of  $9^\circ$ . We estimated the height of this dome with the Ashbrook method, yielding an average slope angle of  $2.7^\circ$  and a height of 230 m, which is found to be in excellent agreement with the photoclinometry and shape from shading analysis. If the height estimates by Brungart (1964) for these three domes were correct, the domes would have to display shadows of length 13.5, 9.9, and 15.7 km in Figs. 2e and 3d, respectively, which is clearly not the case.

Similarly, the height estimates for the domes H1–H6 near Hortensius are systematically higher than ours by a factor of two and more, and for the flank slopes values of up to  $20^\circ$  are stated. In Section 4.5 we have shown a good consistency between images independently acquired under illumination conditions strongly different from those given for the image we used for 3D reconstruction and corresponding synthetic images rendered based on our 3D profiles (Fig. 7). In contrast, the height and slope values given by Brungart (1964) for these domes would imply large shadows of a length of up to 25 km for the domes in Fig. 3a, which do not exist.

From these results we conclude that the height estimates by Brungart (1964) are systematically too high by a significant amount. This finding clearly shows how difficult it is to

measure accurately shadow lengths in high-contrasted photographic reproductions, since shading effects are easily confused with black shadows, leading to a systematic over-estimation of height and slope.

Accurate height measurements of lunar volcanic edifices have been presented by Pike and Clow (1981). Their values are based on the lunar topographic orthophotomaps with a standard elevation error of 30 m. Their data set primarily contains lunar cones, but they have determined the height of one mare dome of our data set, Cauchy  $\omega$ , stating a value of 116 m. The height of 125 m we obtained by means of photogrammetry and shape from shading analysis is in good agreement. For comparison, the corresponding height value by Brungart (1964) of 306 m (entry no. 36) is again too large.

## 5. Analysis of spectral and morphometric properties

This section begins with an overview about previous classification schemes for lunar domes, which are essentially based on morphology and a few approximate morphometric quantities. Subsequently, we will examine interdependencies between the examined spectral and morphometric properties of lunar mare domes which will be of importance for deriving a classification scheme and for the geological interpretation of our data. We will group the examined set of lunar mare domes into several classes based on a principal component analysis of their spectral and morphometric features.

### 5.1. Previous classification schemes for lunar domes

The most commonly used classification schemes for lunar domes are those introduced by Westfall (1964) and by Head and Gifford (1980).

The Westfall scheme has primarily been devised for visual observations. It is essentially morphological and it does not yield a true classification because no dome categories are defined. The morphometric quantities taken into account by this scheme are diameter and slope, where the slope is described by the two categories “gentle” (lower than  $2^\circ$ ) and “moderate” (between  $2^\circ$  and  $5^\circ$ ). According to the Westfall scheme several important morphologic characteristics such as the overall shape of the dome and the presence and position of a summit crater pit are summarized in an alphanumeric string.

Head and Gifford (1980) define seven classes of lunar domes. Classes 1, 2, and 3 refer to volcanic features resembling terrestrial shield volcanoes. Class 1 domes have circular to elliptical outlines, their diameters are between 5.5 and 15 km, they exhibit slopes smaller than  $5^\circ$ , and they have summit craters without raised rims. A typical example is H2. Class 2 domes differ from class 1 domes essentially by their pancake-like cross-sectional shape. H1 represents an example. The distinction between classes 1 and 2 basically relies on a qualitative estimation of 3D shape. Class 3 domes are similar to those of classes 1 and 2 but exhibit a lower topographic relief. The low domes near Cauchy are good examples of this class. Class 4 denotes domes associated with mare ridges and arches, which

may be of tectonic origin, while class 5 describes domes originating from lava mantling of pre-existing highland topography. Class 6 includes domes with higher albedo than mare material and comparably steep slopes, like Gruithuisen  $\gamma$  and  $\delta$ . Class 7 describes complex mare domes with irregular outline and topography, such as A2 and A3 (Arago  $\alpha$  and  $\beta$ ) and many of the domes observed in the Marius Hills region. The morphometric features taken into account by this classification scheme are the approximate dome diameter and a rough estimate of flank slope.

Both classification schemes are mainly based on a qualitative description of dome shape and its geologic setting rather than morphometric quantities. Especially the assignment of a dome to Head and Gifford classes 1, 2, or 3, which are important as they denote mare domes which are isolated from other volcanic features, will remain ambiguous in many cases. Hence, in this section we will devise a classification scheme which is complementary to the scheme introduced by Head and Gifford (1980) in that it subdivides lunar mare domes, especially those belonging to their classes 1–3, according to the spectral and morphometric properties in a quantitative way.

### 5.2. Interdependencies between the determined lunar dome properties

#### 5.2.1. Spectral properties

The Clementine UV–vis multi-spectral image data were obtained at five wavelengths: 415, 750, 900, 950, and 1000 nm. We utilize the Clementine global mosaic generated by Eliason et al. (Eliason, E., Isbell, C., Lee, E., Becker, T., Gaddis, L., McEwen, A., Robinson, M., 1999. Mission to the Moon: The Clementine UV–vis global mosaic. PDS Volumes USA\_NASA\_PDS\_CL\_4001 4078. <http://pdsmaps.wr.usgs.gov>). In this data set, the corresponding UV–vis reflectances are normalized to an incidence angle of  $30^\circ$  and an emission angle of  $0^\circ$ , and calibrated with respect to the laboratory spectrum of Apollo 16 sample 62331. We examined the extracted Clementine UV–vis data in terms of reflectance at 750 nm, denoted by  $R_{750}$ , and the  $R_{415}/R_{750}$  and  $R_{950}/R_{750}$  spectral ratios (Weitz and Head, 1999; cf. also Gaddis et al., 2003). The size of the sample area on the lunar surface was set to  $2 \times 2 \text{ km}^2$ .

Prior to the Clementine mission, the characterization of lunar soil types was performed by means of reflectance spectra measured with Earth-based telescopes (Adams and McCord, 1970; McCord et al., 1972; McCord and Adams, 1973). Reflectance  $R_{750}$  is an indicator of variations in soil composition, maturity, particle size, and viewing geometry. The UV–vis spectral ratio, e.g., given by  $R_{415}/R_{750}$ , is correlated with the variations in  $\text{TiO}_2$  content of mare soils. A characterization of spectral features attributable to titanium in lunar soils is provided by Burns et al. (1976). Through comparison with the analysis of returned lunar samples, the UV–vis ratio reveals for example that the units of highest  $\text{TiO}_2$  content occur in northwestern Mare Tranquillitatis, with decreasingly lower  $\text{TiO}_2$  content in northern Mare Tranquillitatis, south-western Mare Serenitatis, and central Mare Serenitatis (Charette et al., 1974). These results

have been confirmed and refined by subsequent studies of  $\text{TiO}_2$  variations in this region (McCord et al., 1976; Pieters, 1978; Melendrez et al., 1994; Staid et al., 1996). Recent work by Gillis and Lucey (2005), however, relying on  $\text{TiO}_2$  abundance data obtained with the Lunar Prospector neutron spectrometer, indicates that other effects such as ilmenite grain size or FeO content may contribute to the UV–vis ratio. Hence, accurate estimates of the absolute  $\text{TiO}_2$  weight percent values from spectral properties require supporting information beyond the UV–vis spectral ratio, such as reflectance at 2.7  $\mu\text{m}$  and radar backscatter (Gillis et al., 2005). According to these analyses,  $\text{TiO}_2$  content is monotonously increasing with  $R_{415}/R_{750}$  ratio, but the correlation is only moderate and the data display a strong scatter. Gillis and Lucey (2005) establish a trend with a higher slope, valid for  $R_{415}/R_{750}$  ratios of larger than  $\sim 0.62$  and a  $\text{TiO}_2$  content of more than 2 wt%, represented, e.g., by the Mare Tranquillitatis soils, and a distinct second trend with a lower slope, valid for smaller  $R_{415}/R_{750}$  ratios and represented, e.g., by several types of soils in Oceanus Procellarum, termed Procellarum 2, 3, and 5 by Gillis and Lucey (2005).

The  $R_{950}/R_{750}$  color ratio is related to the strength of the mafic absorption band, representing a measure for the FeO content of the soil and being also sensitive to the optical maturity of mare and highland materials (Lucey et al., 1998). Utilizing these albedo and spectral ratio values has become a common approach to the spectrophotometric analysis of Clementine UV–vis data, as it allows for the mutual distinction between different types of basaltic mare soils and highland soils.

The  $R_{750}$  vs  $R_{415}/R_{750}$  diagram (Fig. 8a) illustrates the low 750 nm reflectances and high  $R_{415}/R_{750}$  ratios of the Arago and Cauchy dome fields, showing a largely linear relation between these values. The Hortensius domes display rather large 750 nm reflectances and moderate  $R_{415}/R_{750}$  ratios, while the Milichius domes exhibit moderate 750 nm reflectances and low  $R_{415}/R_{750}$  ratios. The  $R_{750}$  vs  $R_{950}/R_{750}$  diagram (Fig. 8b) shows a linear correlation between 750 nm reflectance and  $R_{950}/R_{750}$  ratio. The brighter lavas of the Hortensius and Milichius domes thus exhibit a slightly stronger mafic absorption (lower  $R_{950}/R_{750}$  ratio) than the low-albedo lavas of the Arago and Cauchy dome fields. The  $R_{950}/R_{750}$  vs  $R_{415}/R_{750}$  diagram (Fig. 8c) illustrates that the  $R_{415}/R_{750}$  ratio increases with decreasing strength of the mafic absorption band.

The spectral signatures shown in Fig. 8 are typical of mare soils of different compositions (cf. Gaddis et al., 2003). The linear relation between  $R_{750}$  and  $R_{950}/R_{750}$  in Fig. 8b ranging from the upper left to the lower right of the diagram indicates that the examined mare soils all have a similar FeO content (Lucey et al., 1998, Fig. 3 therein). The  $R_{750}$  value is higher and the  $R_{950}/R_{750}$  ratio is lower for the domes in Mare Insularum, which indicates that these domes consist of somewhat less mature material than the Mare Tranquillitatis domes. This slight difference in soil maturity may be largely due to the effects of horizontal mixing with bright ray material from the nearby craters Copernicus and Kepler. As a whole, however, all examined domes consist of mare basalts of high maturity. This is supported by the distribution of the data points in the  $R_{750}$  vs  $R_{415}/R_{750}$  plot shown in Fig. 8a, ranging from the upper left to

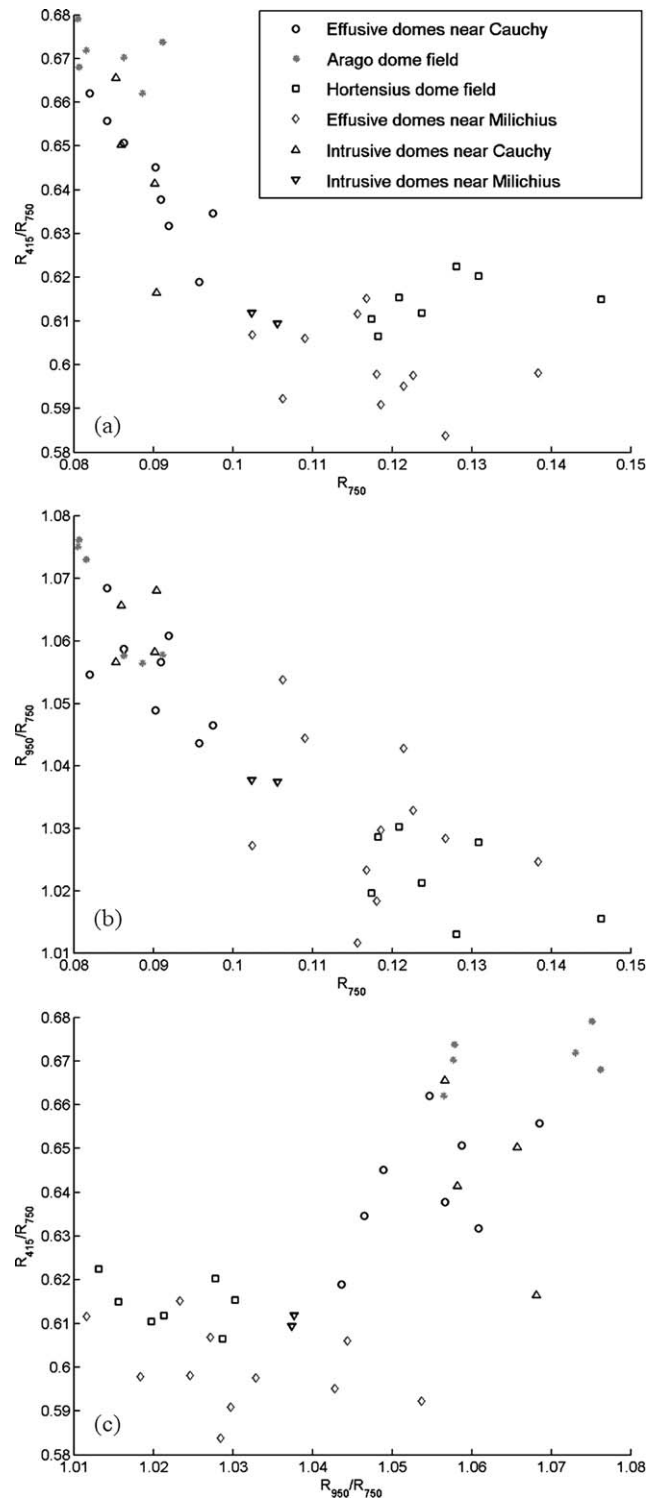


Fig. 8. (a) Reflectance  $R_{750}$  vs spectral ratio  $R_{415}/R_{750}$ . Circles denote the effusive domes near Cauchy and in northern Mare Tranquillitatis, stars the Arago dome field, squares the Hortensius dome field, diamonds the effusive domes near Milichius, up-triangles the intrusive domes near Cauchy, and down-triangles the intrusive domes near Milichius. (b) Reflectance  $R_{750}$  vs spectral ratio  $R_{950}/R_{750}$ . (c) Spectral ratio  $R_{950}/R_{750}$  vs spectral ratio  $R_{415}/R_{750}$ .

the lower right of the diagram, thus indicating significant variations in  $\text{TiO}_2$  content across the data set and an overall high soil maturity (Lucey et al., 1998, Fig. 15 therein).

The fact that the  $R_{415}/R_{750}$  ratio is significantly higher for the dome fields in Mare Tranquillitatis than for those in eastern Oceanus Procellarum can thus be largely attributed to a higher  $\text{TiO}_2$  content of the Mare Tranquillitatis domes. The Tranquillitatis and Procellarum soils are represented by the two distinct trends of  $R_{415}/R_{750}$  vs  $\text{TiO}_2$  content established by Gillis and Lucey (2005), respectively. Due to the weak overall correlation and the strong scatter observed for both trends by Gillis and Lucey (2005), we do not attempt in this work to derive absolute  $\text{TiO}_2$  weight percent values for the lunar mare domes but merely provide qualitative estimates (“low,” “moderate,” “high”) of their  $\text{TiO}_2$  content.

The domes near Arago in western Mare Tranquillitatis are somewhat bluer, i.e., richer in  $\text{TiO}_2$ , than the domes near Cauchy and in northern Mare Tranquillitatis. This is in agreement with the observation by Staid et al. (1996) that the western Mare Tranquillitatis basalts display the highest  $\text{TiO}_2$  content in this region. Most examined domes are indistinguishable from the surface surrounding them, but some, e.g., C5 in northern Mare Tranquillitatis and M12 in Mare Insularum, are distinctly redder than the surrounding mare material (Fig. 2d). This phenomenon will be discussed in more detail in Section 6.

### 5.2.2. Morphometric properties

For a subset of 19 domes we were able to detect a summit crater pit and to measure its diameter  $D_c$ . For the domes H3 and M6 having two crater pits, respectively, only the larger ones were taken into account. We found that  $D_c$  is strongly correlated with the dome diameter  $D$  as shown in Fig. 9a. Linear regression between  $D_c$  and  $D$  yields

$$D_c = 0.12D + 1.17 \quad (8)$$

( $D$  and  $D_c$  in kilometers) with a correlation coefficient of 0.74. As shown in Fig. 9a, our data are consistent with the relation  $D_c = 0.16D + 0.52$  established by Head and Gifford (1980) based on a set of 12 effusive domes, since their relation lies fully inside the one standard deviation confidence interval of Eq. (8).

In Fig. 9b the relation between dome diameter and flank slope is shown. It illustrates that low flank slopes of less than  $2^\circ$  occur over the complete range of diameter values, while larger slopes are only found for diameters smaller than about 13 km. The labels in Fig. 9b denote the dome class, respectively, as described in detail in Section 5.3.2.

Fig. 9c illustrates the relation between flank slope and form factor. Domes with low slopes (smaller than  $2^\circ$ ) may display a variety of shapes, ranging from conical ( $f \approx 1/3$ ), like, e.g., A2 and A3, to parabolic ( $f \approx 0.5$ ) or pancake-shaped ( $f \approx 0.6$ ) like some flat domes in the Milichius field. Domes with slopes larger than  $2^\circ$  are restricted to larger values of  $f$ .

Fig. 10a shows that dome volume does not increase monotonically with flank slope. High volumes are primarily found for low to intermediate slopes between  $1^\circ$  and  $2^\circ$  especially in the Milichius dome field, with the exception of the comparably steep-sided and voluminous domes H5 and H6. Very low edifice volumes are observed for several shallow domes with slopes

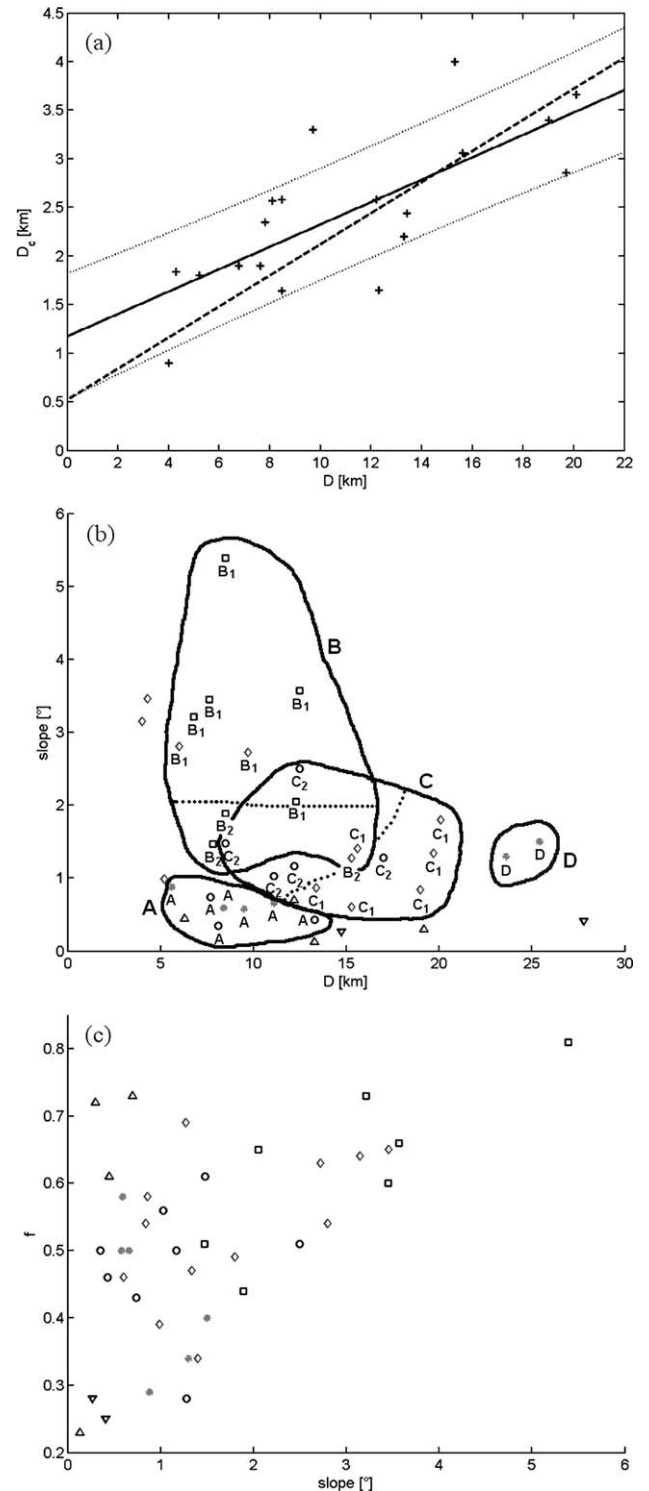


Fig. 9. (a) Crater pit diameter  $D_c$  vs dome diameter  $D$ . The solid line corresponds to the linear fit to our data, the dotted curves to the one standard deviation confidence interval, and the dashed line to the analogous relation established by Head and Gifford (1980). (b) Diameter  $D$  vs flank slope  $\zeta$ . The domes are labeled according to their respective class as defined in Section 5.3. (c) Flank slope  $\zeta$  vs form factor  $f$ .

smaller than  $1^\circ$  in the Cauchy and Arago dome fields and for M8 and M9, two very small but comparably steep domes in the Milichius field.

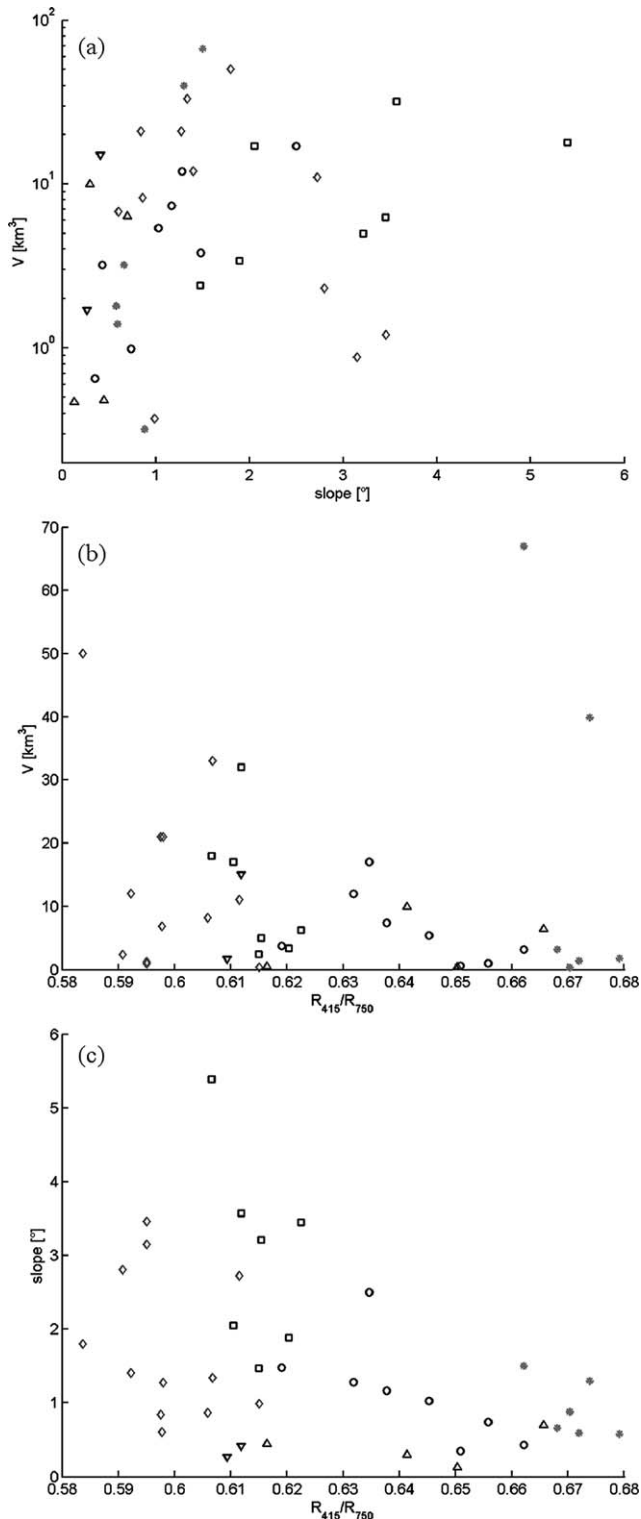


Fig. 10. (a) Flank slope  $\zeta$  vs edifice volume  $V$ . (b) Spectral ratio  $R_{415}/R_{750}$  vs edifice volume  $V$ . (c) Spectral ratio  $R_{415}/R_{750}$  vs flank slope  $\zeta$ .

### 5.2.3. Spectral vs morphometric properties

Fig. 10b shows that low edifice volumes occur for arbitrary  $R_{415}/R_{750}$  ratio and TiO<sub>2</sub> content, while high volumes are only observed for domes with moderate or low TiO<sub>2</sub> content. Hence, the envelope of the data points is decreasing with increasing

$R_{415}/R_{750}$  ratio. The high-TiO<sub>2</sub> and voluminous volcanic edifices A2 and A3 (Arago  $\alpha$  and  $\beta$ ) are exceptional in that they exhibit properties different from those observed for the other high-TiO<sub>2</sub> domes. This indicates fundamentally different mechanisms involved in their formation (cf. Section 6).

We observe a similar relation in the  $R_{415}/R_{750}$  ratio vs flank slope diagram shown in Fig. 10c. Steep slopes (more than 3°) are observed only for the lower  $R_{415}/R_{750}$  ratios, while intermediate and shallow slopes are observed over the complete range of  $R_{415}/R_{750}$  values. No strictly monotonously decreasing envelope of the data points is apparent, however, but only a very general trend. For example, the domes near Arago with  $R_{415}/R_{750} \approx 0.67$  are not shallower than most domes near Cauchy and in northern Mare Tranquillitatis despite the lower  $R_{415}/R_{750}$  ratio (between 0.62 and 0.66) of the latter, while steep slopes of more than 3° already occur for some domes in the Hortensius field with intermediate  $R_{415}/R_{750}$  ratios larger than 0.61. The clearly observed absence of steep domes consisting of high-TiO<sub>2</sub> lava may be related to the influence of metal content on lava viscosity (Melendrez et al., 1994). This issue is further discussed in Section 6.

### 5.3. Classification of lunar mare domes based on their spectral and morphometric properties

#### 5.3.1. Grouping of the domes by principal component analysis

As shown in Table 3, we describe a lunar dome without a summit crater by eight spectral and morphometric features: reflectance  $R_{750}$  at 750 nm wavelength,  $R_{415}/R_{750}$  and  $R_{950}/R_{750}$  reflectance ratios, slope  $\zeta$ , diameter  $D$ , height  $h$ , volume  $V$ , and form factor  $f$ . A subset of 19 domes has a summit crater, and the crater diameter  $D_c$  could be measured. We observed, however, a linear correlation between summit crater diameter  $D_c$  and dome diameter  $D$  (Section 5.2.2), such that taking into account  $D_c$  would not introduce novel information into the analysis. For the crater depth  $d_c$  we could only derive a lower limit but no accurate value, such that the crater depth is also excluded from the analysis.

For a grouping of our set of lunar domes, we thus describe each individual dome by a feature vector  $\vec{v}^{(i)}$  in a space of  $N = 8$  dimensions. To examine the distribution of feature vectors, we make use of the principal component analysis (PCA) as described by Pike (1978). The PCA method is a very common approach in the domain of statistical pattern recognition (Schürmann, 1996). We normalize the  $N = 8$  features to unit variance in order to attribute an equal a-priori importance to each feature. This corresponds to a so-called “whitening transformation” of the feature vectors  $\{\vec{v}^{(i)}\}$  according to

$$\vec{u}^{(i)} = S \cdot (\vec{v}^{(i)} - \vec{m}) \quad (9)$$

with  $\vec{m}$  as the average of all feature vectors  $\{\vec{v}^{(i)}\}$ , and  $S$  as a diagonal matrix with diagonal elements  $S_{nn} = 1/\sigma_n$  ( $n = 1, \dots, N$ ) that denote the reciprocal variances of the  $N$  features. Hence, we describe the data set by the vectors  $\{\vec{u}^{(i)}\}$ , which are of zero mean, and each component is of unit variance. Following the PCA approach, the transformed  $N$ -dimensional feature

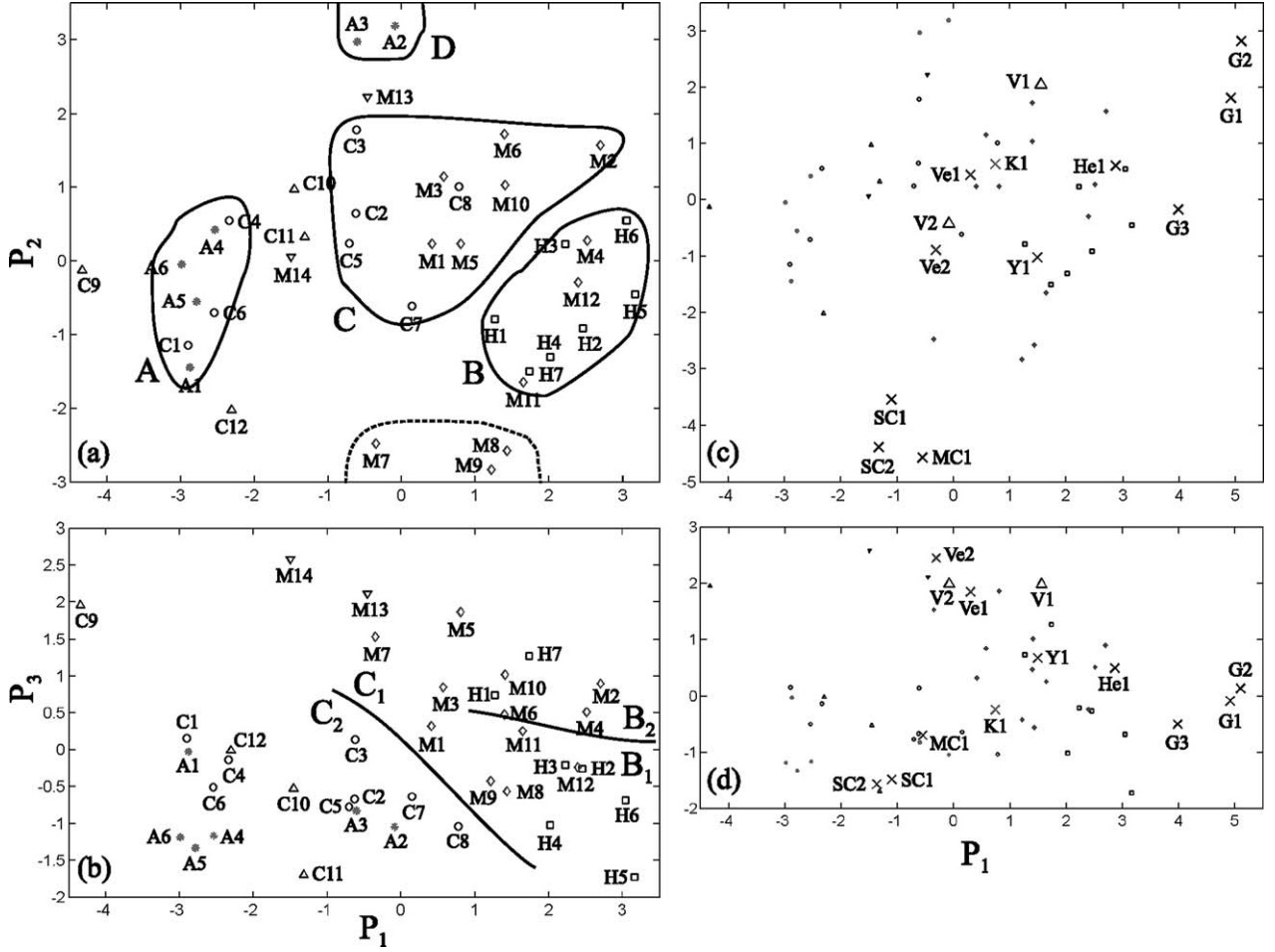


Fig. 11. Classification of lunar mare domes. (a) Scores  $P_1$  and  $P_2$  of the feature vectors describing the domes in the four examined dome fields on the first two principal components of the data distribution. The classes A–D defined in Section 5.3 are indicated. (b) Scores  $P_1$  and  $P_3$  of the same feature vectors on the first and the third principal component. The subdivision of classes B and C into subclasses  $B_1$ ,  $B_2$  and  $C_1$ ,  $C_2$  is indicated. (c) Comparison of the domes in the four examined dome fields to mare domes in other lunar regions, highland domes, and lunar cones, scores  $P_1$  and  $P_2$  on the first two principal components. (d) Scores  $P_1$  and  $P_3$  of the same feature vectors on the first and the third principal component.

vector  $\vec{u}^{(i)}$  obtained according to Eq. (9) and describing dome  $i$  is projected into the  $M$ -dimensional subspace with  $M < N$ , spanned by the eigenvectors  $\{\vec{e}_m\}_{m=1,\dots,M}$  (principal components) of the covariance matrix of the data set that belong to its largest  $M$  eigenvalues  $\{\lambda_m\}_{m=1,\dots,M}$ . The eigenvectors are normalized to unit length. The PCA yields the linear transformation from  $N$ -dimensional feature space into an  $M$ -dimensional subspace with  $M < N$  that minimizes the corresponding loss of information for the given data set. The corresponding vector  $\vec{w}^{(i)}$  which describes dome  $i$  in the  $M$ -dimensional subspace is then given by

$$\vec{w}^{(i)} = (P_1^{(i)}, \dots, P_M^{(i)}) = (\vec{u}^{(i)} \cdot \vec{e}_1, \dots, \vec{u}^{(i)} \cdot \vec{e}_M). \quad (10)$$

In our data set the distributions of the morphometric features  $\zeta$ ,  $D$ ,  $h$ , and  $V$  are strongly skewed towards lower values and thus not normally distributed. Pike (1978) states that these morphometric features are lognormally distributed for the large data set of more than 200 objects examined in his study, which, however, primarily consists of terrestrial volcanoes. Hence, Pike (1978) utilizes the corresponding logarithms instead of the orig-

inal values in order to achieve a more evenly distributed representation of the data set in the reduced subspace spanned by the first  $M$  principal component vectors.

We follow the approach by Pike (1978) and introduce the logarithms of  $\zeta$ ,  $D$ ,  $h$ , and  $V$  into our analysis. This transformation strongly reduces the number of “outliers” with very large absolute scores on the first principal components. For visualization purposes it is advantageous to project the  $N$ -dimensional feature vectors into a subspace with  $M = 2$  dimensions. In the scenario examined here, the loss of information is smaller than 25%. To examine the data distribution in feature space more accurately it turned out to be useful to regard also the score  $P_3$  on the third principal component, leading to an overall loss of information of only 13%. In the plot shown in Fig. 11a, each dome of our data set is represented by the scores  $P_1$  and  $P_2$  on the first two principal components, while Fig. 11b displays the scores  $P_1$  and  $P_3$  on the first and the third principal component, respectively. The average vector  $\vec{m}$  of our data set, the standard deviations  $\sigma_n$ , and the first three principal components  $\vec{e}_1$ ,  $\vec{e}_2$ , and  $\vec{e}_3$  are given in Table 4.

Table 4  
Mean vector  $\vec{m}$  of the feature vectors and standard deviations  $\sigma_n$  of their components, derived from our data set, along with the first three principal components  $\vec{e}_1, \vec{e}_2, \vec{e}_3$

Feature	$\vec{m}$	$\sigma_n$	$\vec{e}_1$	$\vec{e}_2$	$\vec{e}_3$
$R_{750}$	0.1049	0.0180	0.4285	-0.1966	0.3240
$R_{415}/R_{750}$	0.6269	0.0274	-0.3779	0.1468	-0.4379
$R_{950}/R_{750}$	1.0435	0.0185	-0.4268	0.0994	-0.3308
$\lg(\zeta [^\circ])$	0.0460	0.3593	0.4144	-0.1173	-0.3827
$\lg(D [\text{km}])$	1.0415	0.2071	0.0039	0.6825	0.2066
$\lg(h [\text{m}])$	2.0307	0.3531	0.4208	0.2787	-0.2710
$\lg(V [\text{km}^3])$	0.6998	0.6197	0.2941	0.5643	-0.1407
$f$	0.5154	0.1433	0.2370	-0.2327	-0.5581

### 5.3.2. Classes of effusive domes

In Fig. 11a, we will first regard the effusive domes of our set. The Cauchy dome field clearly exhibits two groups:

$$G_C^{(1)} = \{C1, C4, C6\},$$

$$G_C^{(2)} = \{C2, C3, C5, C7, C8\}.$$

Similarly, the Arago dome field consists of the groups:

$$G_A^{(1)} = \{A1, A4, A5, A6\},$$

$$G_A^{(2)} = \{A2, A3\}.$$

The Hortensius dome field is composed of the slightly detached groups:

$$G_H^{(1)} = \{H2, H3, H4, H5, H6\},$$

$$G_H^{(2)} = \{H1, H7\}.$$

The Milichius dome field decomposes into the distinctly separate groups:

$$G_M^{(1)} = \{M4, M11, M12\},$$

$$G_M^{(2)} = \{M1, M2, M3, M5, M6, M10\},$$

$$G_M^{(3)} = \{M7, M8, M9\}.$$

Groups  $G_A^{(1)}$  and  $G_C^{(1)}$  strongly overlap and form a first class A with respect to their similar spectral and morphometric properties:

$$\text{class A: } G_A^{(1)} \cup G_C^{(1)} = \{A1, A4, A5, A6, C1, C4, C6\}.$$

Class A domes are characterized by large  $R_{415}/R_{750}$  ratios corresponding to high  $\text{TiO}_2$  content, small to intermediate diameters between 5 and 13 km, very low flank slopes of less than  $1^\circ$ , and low edifice volumes of no more than  $3 \text{ km}^3$ .

A second class of domes is formed by the overlapping groups  $G_H^{(1)}$ ,  $G_H^{(2)}$ , and  $G_M^{(1)}$ , comprising the Hortensius dome field and certain domes of the Milichius field:

$$\text{class B: } G_H^{(1)} \cup G_H^{(2)} \cup G_M^{(1)} \\ = \{H1, H2, H3, H4, H5, H6, H7, M4, M11, M12\}.$$

Class B domes are characterized by intermediate  $R_{415}/R_{750}$  ratios and thus a moderate  $\text{TiO}_2$  content and intermediate diameters between 6 and 15 km. They cover a broad range of

flank slopes between  $1.3^\circ$  and  $5.4^\circ$ , concentrating around  $3^\circ$ , and have edifice volumes between 2 and  $32 \text{ km}^3$ .

The domes H1 and H7 have low slopes of less than  $2^\circ$ , and dome M4 is similar to them, while the other domes of the Hortensius field are steeper. But with their spectral properties (intermediate  $\text{TiO}_2$  content) and moderate diameters and volumes they nevertheless fit into class B. Hence, an intuitive step is to divide class B into the subclasses  $B_1$  and  $B_2$ :

$$\text{class } B_1: \{H2, H3, H4, H5, H6, M11, M12\},$$

$$\text{class } B_2: \{H1, H7, M4\}.$$

The separation between the subclasses  $B_1$  and  $B_2$  is primarily apparent in Fig. 11b, displaying the scores  $P_1$  and  $P_3$  on the first and the third principal component of our data set.

The domes M7, M8, and M9 (group  $G_M^{(3)}$ ) are separate from class B due to their comparably small diameters of no more than 5 km and their very small edifice volumes of less than  $1.2 \text{ km}^3$ . These domes are less steep than but morphometrically similar to lunar cones like, e.g., Isis and Osiris in Mare Serenitatis (Weitz and Head, 1999, cf. also Fig. 11c).

A third class is made up by the overlapping groups  $G_C^{(2)}$  and  $G_M^{(2)}$ , comprising certain domes of the Cauchy and the Milichius dome fields:

$$\text{class C: } G_C^{(2)} \cup G_M^{(2)} \\ = \{C2, C3, C5, C7, C8, M1, M2, M3, M5, M6, M10\}.$$

Class C covers quite a broad range of  $R_{415}/R_{750}$  ratios as it contains both high- $\text{TiO}_2$  domes in northern Mare Tranquillitatis (consisting, however, of spectrally slightly redder lava than their neighbors of class A) and moderate- $\text{TiO}_2$  domes in the Milichius region. Despite their low flank slope (smaller than  $1.8^\circ$ , excluding the morphologically exceptional dome C8 situated on a mare ridge), their edifice volumes are moderate to large (mostly around  $10 \text{ km}^3$ , up to  $50 \text{ km}^3$ ) due to their large diameters of up to 20 km. Several domes of this class have a flat, pancake-shaped appearance. The class C domes of the Cauchy field are morphometrically similar to but spectrally distinct from the class C domes of the Milichius field, as they consist of high- $\text{TiO}_2$  material. Hence, we suggest a division of class C into two subclasses:

$$\text{class } C_1: G_M^{(2)} = \{M1, M2, M3, M5, M6, M10\},$$

$$\text{class } C_2: G_C^{(2)} = \{C2, C3, C5, C7, C8\}.$$

This subdivision is again apparent in the  $(P_1, P_3)$  plane shown in Fig. 11b and reflects the differences in lava composition between the Cauchy and the Milichius dome fields.

The large and voluminous edifices of the domes A2 and A3 (Arago  $\alpha$  and  $\beta$ ) are assigned to a separate class D:

$$\text{class D: } G_A^{(2)} = \{A2, A3\}.$$

These domes consist of the same high- $\text{TiO}_2$  lava as the nearby smaller class A domes, but their strongly different morphometric properties suggest a different mode of formation (see the discussion in Section 6). A summary of the approximate

Table 5  
Approximate spectral and morphometric properties characterizing the dome classes defined in Section 5.3

Class	TiO <sub>2</sub> content	$\zeta$ [°]	$D$ [km]	$V$ [km <sup>3</sup> ]
A	High	0.3–1.0	5–13	<3
B <sub>1</sub>	Moderate	2.0–5.4	6–15	5–32
B <sub>2</sub>	Moderate	1.3–1.9	8–15	2–21
C <sub>1</sub>	Low to moderate	0.6–1.8	13–20	7–50
C <sub>2</sub>	Moderate to high	1.0–2.5	8–17	4–17
D	High	1.3–1.5	≈25	40–67

spectral and morphometric properties characterizing the dome classes defined in this section is given in Table 5.

We found that except for a small number of domes, the distribution of the data set in ( $P_1$ ,  $P_2$ ) space does not change significantly when the three spectral features are omitted in the principal component analysis. One of the exceptions is M7, which is very similar to the class A domes with respect to its morphometric properties but consists of spectrally much redder material. Similarly, neglecting spectral properties makes the distinction between subclasses C<sub>1</sub> and C<sub>2</sub> disappear, and the classes B and C exhibit a mutual overlap. In Fig. 9b, the classes are displayed in the merely two-dimensional diameter vs flank slope subspace. These values are the morphometric parameters that can be derived most easily, even without full 3D reconstruction (cf. Section 4.1). In this diagram, classes A and D can be fully separated from classes B and C. Classes B and C, however, strongly overlap, such that domes with diameters between 8 and 16 km and flank slopes between 1.3° and 2.5° cannot be assigned unambiguously to classes B or C. The subdivision of class B into subclasses B<sub>1</sub> and B<sub>2</sub> is apparent, since it is mainly due to flank slope, while the subdivision of class C into C<sub>1</sub> and C<sub>2</sub> is less obvious as it is to a large extent due to spectral properties. Dome M7 is near class A because of its similar morphometric properties. Domes M8 and M9 are near class B<sub>1</sub>, mainly because their very low volume is not taken into account here. On the whole, the diameter vs flank slope subspace may be used for the purpose of preliminary classification if no further morphometric or spectral data are available.

### 5.3.3. Comparison to the Head and Gifford scheme

In comparison to the classification scheme by Head and Gifford (1980), we found that our class A domes are mainly of their class 3, displaying very shallow profiles. Most of our class B<sub>1</sub> domes are of Head and Gifford class 1 due to their comparably steep slopes (e.g., H2, H4, M12), while the shallower class B<sub>2</sub> domes in our data set, which are not all represented in the set analyzed by Head and Gifford (1980), can be assigned to their class 2 (e.g., H1, H7). Most of the shallow domes of our data set that belong to class C can be assigned to Head and Gifford class 2 due to their low and in some cases pancake-like cross-sectional shape (e.g., C2, M3), while the shallower members of class C<sub>2</sub> (e.g., C3, C5, C7) are rather of their class 3.

Head and Gifford classes 4–6 are purely morphologic classes, i.e., the assignment of a dome to one of these classes is based on its geologic and morphologic setting and its qualitative appearance rather than morphometric values. Their class 7

describes large and complex edifices such as A2 and A3 (Arago  $\alpha$  and  $\beta$ ) as well as structures in the Marius Hills regions and thus comprises our class D.

The classification scheme presented in this section is complementary to the scheme by Head and Gifford (1980) in that it bases the distinction between the domes belonging to their classes 1–3 on spectral and morphometric quantities.

### 5.3.4. Intrusive domes

A further class of lunar domes are the intrusive domes or “lava swells,” which were formed by subsurface intrusions of lava rather than lava effusion (Head and Gifford, 1980). Subsurface accumulations of magma caused an up-doming of the bedrock layers and created a smooth, gently sloping positive relief, similar to terrestrial laccoliths. These domes do not possess a summit crater pit, their outline may be quite irregular, and they are spectrally indistinguishable from the mare surface surrounding them. Many intrusive domes have larger diameters than typical effusive domes, while they show very gentle flank slopes of usually less than 1°. Hence, they can only be observed when situated extremely close to the lunar terminator.

According to Fig. 10c, the slope of the intrusive domes in our data set is independent of their  $R_{415}/R_{750}$  ratio. The shallowest dome we have examined is M14 with a slope of less than 0.3°; presumably, intrusive domes with even more gentle slopes exist but are extremely difficult to observe. With their morphometric properties, the intrusive domes of our data set lie between the previously defined classes of effusive domes (Fig. 11), supporting the assumption of a different mode of formation. Since we have observed only six intrusive domes in the four dome fields examined in this study, no general conclusion about the distribution of their spectral and morphometric properties can be drawn at present.

### 5.3.5. Comparison to lunar volcanic features in other lunar regions

In order to examine if the devised classification scheme is also representative for domes in other lunar regions, we have placed several effusive domes for which morphometric measurements were available (cf. Fig. 12 and Table 3) into the diagrams in Figs. 11a and 11b. The results are presented in Figs. 11c and 11d.

The well-studied mare dome Kies  $\pi$  (Wöhler and Hafezi, 2005), situated west of the lava-flooded crater Kies in western Mare Nubium, belongs to class C<sub>1</sub> with a tendency towards class C<sub>2</sub>, displaying a low profile, high volume, and moderate to high  $R_{415}/R_{750}$  ratio. Another classical mare dome, Herodotus  $\omega$  situated south-west of crater Aristarchus, with its moderate to steep slope, rather large diameter and volume, and moderate  $R_{415}/R_{750}$  ratio, falls within class B<sub>1</sub>. Due to the fact that it is covered with immature ejecta from the nearby crater Aristarchus, it displays a strong mafic absorption band corresponding to a low  $R_{950}/R_{750}$  ratio. Two shallow domes with large diameters in eastern Mare Fecunditatis near crater Vendelinus (Lena et al., 2005a) which consist of low-TiO<sub>2</sub> material can be assigned to class C<sub>1</sub>. A slightly steeper dome with

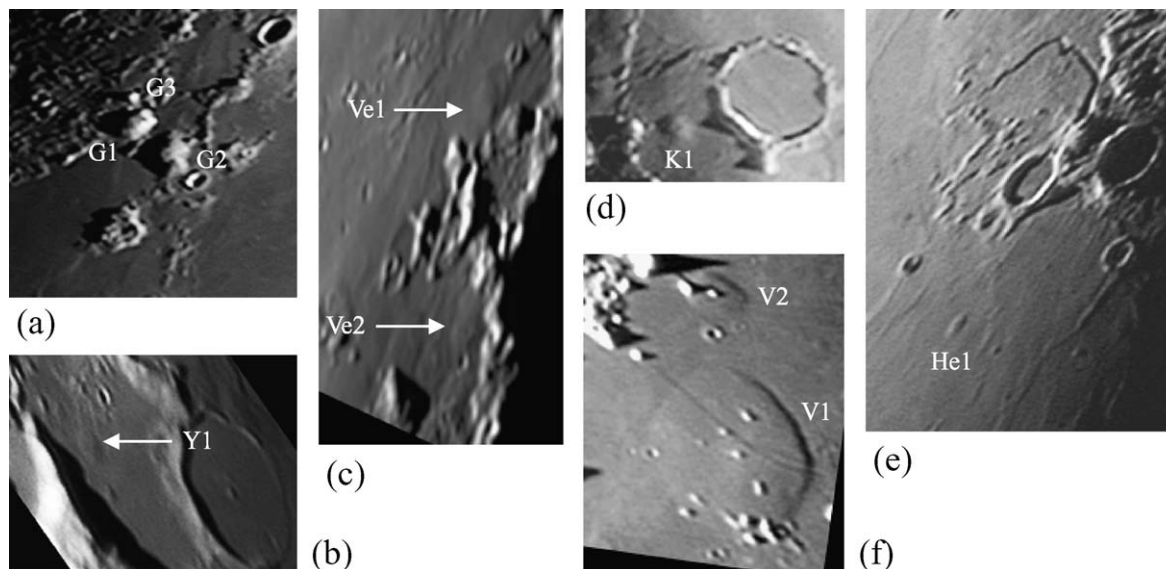


Fig. 12. Domes examined for comparison (cf. also Table 1). (a) Gruithuisen highland domes. (b) Mare dome near Yerkes. Image by C. Fattinanzi. (c) Mare domes near the western rim of Vendelinus. (d) Mare dome Kies  $\pi$ . (e) Mare dome Herodotus  $\omega$ . (f) Valentine dome and its northern neighbor. Image by K.C. Pau.

a smaller diameter, situated near the crater Yerkes in western Mare Crisium (Lena et al., 2005b) clearly falls within class B<sub>2</sub>.

The well-known highland domes Gruithuisen  $\gamma$  and  $\delta$  (Chevrel et al., 1999) have larger diameters, volumes, and flank slopes than all mare domes regarded in this study. The nearby smaller Northwest dome is also very steep. Since we derived the height values reported in Table 3 by shadow length measurement in Fig. 12a, such that no full 3D profile is available, we have assumed a parabolic shape with  $f = 0.5$  according to Wilson and Head (2003) to estimate their volumes. The Gruithuisen domes may have been formed by viscous lava of very low TiO<sub>2</sub> content (corresponding to a very low  $R_{415}/R_{750}$  ratio) and more silicic composition, presumably prior to the lava flooding of the Imbrium basin. Not surprisingly, these highland domes do not fall into any of our previously defined classes of lunar mare domes (Fig. 11c).

Lunar cones with their very small diameters of only a few kilometers and comparably steep slopes of 3° and more make up a group of their own. Here they are represented by a cone near Milichius denoted by MC1 in Table 3, which is the western object of a pair of cones recently described by Viegas et al. (2005), and by the well-known cones Osiris and Isis (SC1 and SC2 in Table 3) situated at the border between Mare Tranquillitatis and Mare Serenitatis. The diameter of MC1 was measured in a Lunar Orbiter high-resolution image, while its height was determined with the shadow length method in the telescopic image in Fig. 3d. The morphometric data for Osiris and Isis were adopted from Pike and Clow (1981). The volumes of the three cones were computed according to the empirical relation  $V_{\text{cone}} = 0.408hD^2$  established by Wood (1979), corresponding to a form factor of  $f = 0.52$ . Volcanic cones are constructed by the accumulation of pyroclastic materials like cinder and ash around a vent, in association with Strombolian, Hawaiian, and Vulcanian eruptions. The presence of lunar pyroclastic constructs implies that gas may be released from the erupted magma, causing disruption of the magma and subsequent dis-

persal of the clasts (Weitz and Head, 1999). Fig. 11c suggests that the domes M7, M8, and M9 with their small diameters might represent intermediate objects between lunar domes and cones.

As a classical example of an intrusive dome we also examined the Valentine dome situated in western Mare Serenitatis, along with a smaller intrusive dome immediately to its north, recently described by Lena et al. (2005c). In Fig. 11, both domes are near the margin of class C<sub>1</sub> and resemble the intrusive domes M13 and M14, respectively.

For illustration, the images of all mare domes examined in this study, rectified to simple cylindrical projection and arranged according to their respective class, are shown in Fig. 5 at uniform scale.

## 6. Results and discussion

### 6.1. Synopsis of spectral and morphometric characteristics

We have observed a large variety of spectral characteristics and 3D shapes of lunar mare domes in the examined four dome fields. We have divided the domes into four classes, two of which we further splitted into two subclasses, respectively.

The dome field situated around Cauchy and in northern Mare Tranquillitatis contains objects of shallow slope and moderate diameter (C2, C3, C5–C8), situated in the moderate to high-TiO<sub>2</sub> unit denoted T<sub>h</sub> by Staid et al. (1996). These domes might be source vents of the T<sub>h</sub> unit, which was later covered by lavas still richer in TiO<sub>2</sub>, denoted by T<sub>vh-B</sub>. The extremely shallow effusive domes C1 and C4, which we assigned to class A, consist of T<sub>vh-B</sub> material and possibly represent source vents of this unit.

The domes in the Arago region are all part of the unit richest in TiO<sub>2</sub>, denoted T<sub>vh-A</sub> by Staid et al. (1996). These domes might represent source vents of this basaltic layer, which is still richer in TiO<sub>2</sub> than the T<sub>vh-B</sub> unit. The morphometric charac-

teristics of the domes A1, A4, A5, and A6 are similar to those of C1 and C4, such that we assigned them to class A as well. The domes A2 and A3 (Arago  $\alpha$  and  $\beta$ ), however, make up a class of their own (class D) according to their large diameters and volumes.

In the Hortensius region, domes of moderate to steep slope covering a wide range of volumes can be found. They are all part of a moderate-TiO<sub>2</sub> basaltic unit, and we have classified all of them as class B. Domes H2–H6 were assigned to subclass B<sub>1</sub> according to their steep slopes and moderate to high volumes; as a general trend, edifice volume is larger for the northern domes than for the southern domes. Domes H1 and H7 with their shallower slopes and lower volumes were assigned to subclass B<sub>2</sub>. The domes H5 and H6 are by far the steepest mare domes examined in this study, with flank slopes of up to 5.4°, and they are among those with the highest volumes.

The domes in the Milichius dome field display a rich variety of 3D shapes. Several domes (M1, M2, M3, M5, M6, M7, M10) have large diameters and shallow to moderate slopes, resulting in pancake-like cross-sections and high volumes. They are part of a basaltic unit of low to moderate TiO<sub>2</sub> content. They are morphometrically similar to but spectrally different from the domes near Cauchy and in northern Mare Tranquillitatis, such that we assigned them to class C<sub>1</sub>. With their smaller diameters and steeper slopes, domes M4, M11, and M12 (Milichius  $\pi$ ) resemble domes of the Hortensius field, such that we assigned them to class B<sub>1</sub>. M11 consists of spectrally very red low-TiO<sub>2</sub> material, similar to that of the highland domes Gruithuisen  $\gamma$  and  $\delta$ , such that it is possibly a highland dome. Its close proximity to the rugged highland terrain west of Tobias Mayer B supports this idea. The dome M7 is morphometrically similar to the small, shallow, low-volume class A domes of the Cauchy and Arago dome fields but consists of spectrally very red material. M8 and M9 are also small and spectrally red but steeper than M7. Their diameters, however, are still twice as large as the diameter of the nearby lunar cone MC1, while they display somewhat shallower flank slopes.

The classification scheme we devised for the examined four dome fields appears to represent domes in other lunar regions as well. For example, the classical mare domes Kies  $\pi$  and Herodotus  $\omega$  and a dome near crater Yerkes in Mare Crisium can clearly be recognized as belonging to class C<sub>1</sub>, B<sub>1</sub>, and B<sub>2</sub>, respectively, distinctly showing the corresponding specific spectral and morphometric properties. Two large but very shallow domes in Mare Fecunditatis lie at the margin of class C<sub>1</sub>, being spectrally similar to but still shallower than the typical representatives of this class, thus somewhat extending the range of class C<sub>1</sub>. Highland domes and cones form groups of their own, indicating that their spectral and morphometric properties are fundamentally different from those observed for mare domes. The well-known intrusive Valentine dome and its smaller neighbor turn out to differ substantially from the effusive mare domes with respect to their morphometric properties, just like the intrusive domes observed in the Cauchy and Milichius dome fields. In the ( $P_1$ ,  $P_2$ ) and ( $P_1$ ,  $P_3$ ) diagrams (Fig. 11) they are broadly distributed between classes A and C, corresponding to moderate to large diameters, very shallow

slopes, and a broad range of volumes and spectral properties. Further morphometric data are necessary to better constrain the limits of their distribution.

Most domes are formed out of the same lava as observed around them and are thus spectrally indistinguishable from their surrounding. Some domes, however, appear to be older than the material around them and were embayed by lava of different composition. For example, dome C5, which is part of the moderate to high-TiO<sub>2</sub> unit T<sub>h</sub> in Mare Tranquillitatis (Staid et al., 1996), is surrounded by spectrally bluer T<sub>vh-B</sub> lava which presumably embayed this dome (Fig. 2d). The dome M12 (Milichius  $\pi$ ) is surrounded by spectrally somewhat bluer lava, and also A2 (Arago  $\alpha$ ) is spectrally slightly redder than its surrounding. A similar relation can be observed for domes C2 and C3 (Cauchy  $\tau$  and  $\omega$ ), but there the outline of the spectrally bluer T<sub>vh-B</sub> lava layer is more irregular.

An order-of-magnitude estimate of the thickness of the uppermost lava flow can be inferred from our dome height measurements. For a dome of diameter  $D$  and height  $h$ , a thickness  $d$  of the embaying lava layer implies a diameter  $D(1 + d/h)$  of the original edifice, assuming a constant flank slope. Hence, lava layer thicknesses of more than 100 m would yield original diameters larger than 25 km which are atypical of effusive lunar mare domes (cf. Section 5.2.2 and Fig. 9b). We conclude that the surrounding spectrally bluer lava layers must be very thin, probably measuring less than 100 m and possibly only some tens of meters. Hiesinger et al. (2003) report similar thicknesses of lava flows of some tens of meters, derived by various authors from shadow measurements, in situ observations of flow units, and studies of the chemical kinetic aspects of lava emplacement and cooling.

## 6.2. Physical parameters of dome formation

The distribution of lunar volcanic domes and their spectral diversity provide insight into the source regions and conditions of ancient volcanic eruptions on the Moon. Studies of active terrestrial volcanism indicate that factors governing the morphology of volcanic edifices are complex. The evolution of a lava dome is controlled predominantly by its effusion rate and rheology. Magma contains silicates, and the amount of SiO<sub>2</sub> controls the viscosity due to polymerization of molecules. This means that they cluster and form larger complexes by repeated linking of identical molecular groups. The more bonds there are, the more viscous the magma is. The high fluidity of Hawaiian lavas is mainly caused by its basaltic composition, characterized by a high Fe, Mg, Ca, and Ti content and a low Si, Al, Na, and K content, compared to highly viscous lavas like the dacite erupted explosively at Mount St. Helens in 1980.

Because of the low silica and alumina content and high iron and titanium content the lunar basalt lavas had a higher temperature, lower viscosity, and higher density than terrestrial basalt lavas (Williams et al., 2000). Temperature has a strong influence on viscosity: as temperature increases, viscosity decreases, an effect particularly evident in the lava flows. For example, an increase in temperature from 1100 to 1300 °C decreases the viscosity of basaltic lava by an order of magnitude (Spera, 2000).

This decrease in viscosity is attributed to an increase in distance between cations and anions, and therefore to a decrease in Si–O bond strength. At temperatures below the beginning of crystallization, viscosity also increases with time for an increasing proportion of crystals. Gases are easily released from low viscosity substances. In more viscous magmas, gases are not released easily, and build up. When the pressure increases, a violent eruption can occur.

The length of a lava flow is a function of velocity and cooling rate (Murase and McBirney, 1970). Since silicic magmas are usually highly viscous, they tend to form the shortest and thickest of all flows. The length of a lava flow is determined by the magma effusion rate. A high effusion rate, where lava spreads rapidly from the vent, usually results in a single flow unit. A low effusion rate, in contrast, results in lavas of limited extent that pile up layer by layer, a mechanism possibly responsible for the formation of Arago  $\alpha$  and  $\beta$ .

The lunar steep-sided highland domes Gruithuisen  $\gamma$  and  $\delta$  appear similar to the terrestrial features characterized by viscous lavas. Furthermore, they are spectrally red structures with an extremely low  $R_{415}/R_{750}$  ratio and have been inferred to be domes formed by silica-rich lavas at the beginning of the late Imbrian epoch 3.85–3.7 Ga ago (Head et al., 2002). The absence of steep domes for high  $R_{415}/R_{750}$  ratios can partly be explained by the influence of metal content on lava viscosity, where higher metal content implies less viscous fluid lavas, and in turn on edifice slope. However, the fact that shallow domes are found independent of their TiO<sub>2</sub> content suggests that further physical parameters of the lava effusion process, probably varying on regional scales, were relevant during dome formation. We will further examine the correlation between TiO<sub>2</sub> content and lava viscosity later in this section.

It is widely accepted that sinuous rilles represent eruptions characterized by very high effusion rates, while mare domes have presumably been formed at much lower effusion rates (Whitford-Stark and Head, 1977). The general assumption is that dome-forming eruptions are characterized by lower effusion rates than eruptions which generate long lava flows. Lower lava temperatures leading to increased lava viscosity may also favor dome formation. Moreover, laboratory simulations, measurements from active and prehistoric flows, and dimensional analysis were used to explore how effusion history and cooling rate affect the final geometry of a dome (Fink and Bridges, 1995). Experiments conducted with polyethylene glycol wax demonstrated that, when the wax cooling rates exceeds a critical minimum value, the flank slope of the artificial dome increases steadily with erupted volume in the course of a single experiment. Therefore the steeper domes represent the result of cooler, more viscous magmas with high crystalline content, perhaps at the final stages of the eruption (Weitz and Head, 1999). Our morphometric data suggest that some domes may have formed from relatively viscous lavas extruded either episodically or at effusion rates low enough to allow the solidified surface crust to exert a dominating influence on the final morphology. Low-TiO<sub>2</sub> domes may have both low and high volumes, while high-TiO<sub>2</sub> domes only have small volumes. Exceptions

are Arago  $\alpha$  and  $\beta$ , consisting of high-TiO<sub>2</sub> lava but having a very high volume.

The lunar mare domes of our data set are fairly symmetrical. Hence, it is appropriate to assume that they were formed by extrusion of magma onto a flat plane spreading in all directions from the vent, in contrast to lava flows resulting from lava extrusion onto an inclined surface. A quantitative treatment of such dome-forming eruptions is given by Wilson and Head (2003), whose approach we will follow here. In their rheologic model, the cooling magma is treated as a Bingham plastic characterized by the yield strength  $\tau$  and the plastic viscosity  $\eta$ . The yield strength is given by

$$\tau = \frac{0.323h^2\rho_0g}{D/2}, \quad (11)$$

where  $\rho_0$  is the lava density, for which Wilson and Head (2003) assume and justify a value of 2000 kg m<sup>-3</sup>,  $g = 1.63$  m s<sup>-2</sup> the acceleration due to gravity,  $h$  the height of the dome, and  $D$  its diameter. The plastic viscosity can be estimated by the empirical relation

$$\eta(\tau) = 6 \times 10^{-4}\tau^{2.4}, \quad (12)$$

where  $\tau$  is expressed in Pa and  $\eta$  in Pa s. An estimate of the lava effusion rate  $E$  is obtained based on the assumption that the advance of the front of a flow unit is limited by cooling once a critical depth of penetration of the cooled boundary layer into the flow is reached. For a dome with a parabolic cross-section (form factor  $f = 0.5$ ), Wilson and Head (2003) derive the expression

$$E = \frac{0.323^{1/2}300\kappa(D/2)^2}{0.65^{5/2}0.72h}, \quad (13)$$

with  $\kappa \approx 10^{-6}$  m<sup>2</sup> s<sup>-1</sup> as the thermal diffusivity of the lava and  $E$  measured in m<sup>3</sup> s<sup>-1</sup>. The duration  $T$  of the lava effusion process amounts to  $T = V/E$ . Equations (11)–(13) are valid for domes that formed from a single flow unit (monogenetic volcanoes). Otherwise, the computed values for  $\tau$ ,  $\eta$ , and  $E$  are upper limits to the respective true values.

We believe that a monogenetic mode of origin can be assumed for nearly all effusive domes of the four examined dome fields, due to their fairly uniform surface texture showing no traces of individual lava flow units or other signs of several subsequent eruption stages. Exceptions are the highly complex edifices Arago  $\alpha$  and  $\beta$  making up class D, which have relatively gentle slopes (1.5° and 1.3°), large diameters (>20 km), and high volumes (>30 km<sup>3</sup>). Likely they formed over a long period of time, compared to the other domes in that region, during which the lava poured out more or less continuously, forming a high volume edifice. This is supported by their morphology with complex surface detail, implying a variety of individual flow units. Image data of higher resolution under oblique illumination are required to examine in detail the structure of these lava flow units. This would allow for a subdivision of the edifices into various layers along with an estimation of their respective thicknesses as described by Wilson and Head (2003) for the Gruithuisen highland domes. The corresponding rheologic properties of each layer could then be determined accordingly. We leave this issue for future studies and exclude Arago

Table 6  
Rheologic properties (viscosity  $\eta$ , effusion rate  $E$ , duration  $T = V/E$  of the effusion process) of the examined lunar domes

Dome	Class	$\eta$ [Pa s]	$E$ [ $\text{m}^3 \text{s}^{-1}$ ]	$T$ [years]
C1	A	$1.22 \times 10^2$	456	0.05
C2	C <sub>2</sub>	$1.04 \times 10^5$	207	1.13
C3	C <sub>2</sub>	$3.49 \times 10^5$	264	1.44
C4	A	$1.04 \times 10^3$	615	0.17
C5	C <sub>2</sub>	$4.45 \times 10^4$	214	0.8
C6	A	$3.85 \times 10^3$	206	0.15
C7	C <sub>2</sub>	$1.34 \times 10^5$	114	1.06
C8	C <sub>2</sub>	$3.94 \times 10^6$	101	5.36
A1	A	$4.98 \times 10^3$	121	0.08
A4	A	$5.63 \times 10^3$	329	0.31
A5	A	$1.88 \times 10^3$	273	0.16
A6	A	$2.32 \times 10^3$	314	0.18
H1	B <sub>2</sub>	$4.27 \times 10^5$	89	1.21
H2	B <sub>1</sub>	$5.97 \times 10^6$	44	4.54
H3	B <sub>1</sub>	$1.53 \times 10^6$	120	4.51
H4	B <sub>1</sub>	$3.17 \times 10^6$	42	3.77
H5	B <sub>1</sub>	$6.60 \times 10^7$	31	18.27
H6	B <sub>1</sub>	$2.30 \times 10^7$	70	14.57
H7	B <sub>2</sub>	$1.03 \times 10^5$	106	0.72
M1	C <sub>1</sub>	$2.84 \times 10^4$	312	0.83
M2	C <sub>1</sub>	$2.85 \times 10^6$	219	7.23
M3	C <sub>1</sub>	$4.29 \times 10^5$	223	1.71
M4	B <sub>2</sub>	$2.63 \times 10^5$	239	2.78
M5	C <sub>1</sub>	$7.07 \times 10^3$	509	0.42
M6	C <sub>1</sub>	$6.13 \times 10^5$	293	3.57
M7		$5.95 \times 10^3$	104	0.11
M8		$1.53 \times 10^6$	25	1.54
M9		$8.15 \times 10^5$	25	1.1
M10	C <sub>1</sub>	$6.17 \times 10^4$	448	1.49
M11	B <sub>1</sub>	$1.37 \times 10^6$	42	1.75
M12	B <sub>1</sub>	$3.36 \times 10^6$	71	4.91
G1		$3.20 \times 10^8$	119	38
G2		$9.70 \times 10^8$	50	38.7
			24	23.8
G3		$9.90 \times 10^8$	24	23.8
			6	9.1
Y1	B <sub>2</sub>	$9.97 \times 10^4$	146	1.05
Ve1	C <sub>1</sub>	$5.65 \times 10^3$	613	0.37
Ve2	C <sub>1</sub>	$8.61 \times 10^1$	1056	0.06
K1	C <sub>1</sub>	$2.61 \times 10^5$	201	2.05
He1	B <sub>1</sub>	$1.30 \times 10^6$	157	4.25
SC1		$3.90 \times 10^5$	13	0.39
SC2		$3.25 \times 10^5$	9	0.28
MC1		$3.27 \times 10^5$	9	0.27

The values for the Gruithuisen domes are from Wilson and Head (2003); for G2 they represent the lower and upper north-western part and for G3 the lower and upper part, respectively.

$\alpha$  and  $\beta$  from the rheologic analysis in this section. The values of  $\eta$ ,  $E$ , and  $T$  we computed for our data set are presented in Table 6.

Domes of class A, consisting of basalt with large  $R_{415}/R_{750}$  ratios and thus high  $\text{TiO}_2$  content, have shallow flank slopes ( $<1^\circ$ ) and low volumes ( $<3 \text{ km}^3$ ). They have been formed out of rather fluid lavas with viscosities between  $10^2$  and  $10^4$  Pa s, extruding at high rates between 100 and  $600 \text{ m}^3 \text{ s}^{-1}$  over short periods of time of no more than a few months. These domes of the Arago and Cauchy dome fields are spectrally similar to

but morphometrically distinct from those of class C<sub>2</sub> (C2, C3, C5, C7, C8) and class D (Arago  $\alpha$  and  $\beta$ ), respectively. The low topographic relief and slope of the class A domes is due to their low lava viscosity implying a high effusion rate.

Domes of class C<sub>2</sub> are characterized by gentle flank slopes, moderate volumes (between  $3.8$  and  $17 \text{ km}^3$ ), and edifices which are higher than those of class A. They originate from moderately viscous lavas with  $\eta$  between  $10^4$  and  $10^7$  Pa s. The corresponding effusion rates between 100 and  $300 \text{ m}^3 \text{ s}^{-1}$  are comparable to those estimated for the class A domes, but the class C<sub>2</sub> domes were formed over longer periods of time between about 0.8 and 5 years.

Class C<sub>1</sub> includes several domes in the Milichius region characterized by a moderate  $\text{TiO}_2$  content and a flat, pancake-shaped appearance with shallow slopes of less than  $2^\circ$ . Interestingly, this class contains both low to intermediate and high volume edifices, such as M1, M3, and M5 with volumes smaller than  $12 \text{ km}^3$  and M2, M6, and M10 with volumes larger than  $20 \text{ km}^3$ . Their low slopes and flat appearances suggest high effusion rates of the erupted lavas ( $E$  between 200 and  $500 \text{ m}^3 \text{ s}^{-1}$ ), where the lower volume of the smaller domes can mainly be attributed to a shorter duration of the effusion process (5 months for M5 compared to more than 7 years for M2). The lava viscosity of the class C<sub>1</sub> domes spans a broad range from about  $6 \times 10^3$ – $3 \times 10^6$  Pa s.

The morphometric properties derived for the domes of class B suggest that dome morphology is directly related to lava viscosity for edifices of similar lava composition, like in the Hortensius dome field. For all Hortensius domes, eruption rates between  $30$  and  $120 \text{ m}^3 \text{ s}^{-1}$  were estimated. However, the steeper and hemispherically shaped class B<sub>1</sub> domes mainly formed out of lava of higher viscosities between  $10^6$  and  $10^8$  Pa s and over longer periods of time (mainly around 4 years, up to 18 years for the high-volume edifices H5 and H6) than the shallower class B<sub>2</sub> edifices H1 and H7, having formed from lavas not more viscous than several  $10^5$  Pa s over periods of time of only about 1 year. The formation conditions of M4, M11, and especially M12 (Milichius  $\pi$ ) are supposedly similar to those encountered in the Hortensius dome field, regarding the observed spectral and morphometric properties and the similarities in the estimated rheologic parameters. Possibly these domes formed simultaneously with the Hortensius domes.

As a whole, the Milichius dome field shows a remarkable variety of dome shapes and thus eruption conditions. It contains voluminous pancake-shaped edifices formed by high effusion rates, steeper domes of moderate size built up by comparably viscous and slowly extruding lavas, very small objects that morphometrically resemble lunar cones, and a typical lunar cone.

For comparison, the Gruithuisen highland domes form a further separate spectral and morphometric group due to their steep flank slopes, high volumes, and red spectral signatures, giving rise to the assumption that they have been formed by lava of significantly different composition erupted at low effusion rates over a long period of time. The analysis by Wilson and Head (2003) reveals that they have been formed by several distinct eruption events. As a further comparison, we examined the typical lunar cones MC1, SC1 (Osiris), and SC2 (Isis),

which are characterized by comparably steep slopes of  $3^\circ$  and more, small diameters, and very low volumes, displaying low eruption rates of only about  $10 \text{ m}^3 \text{ s}^{-1}$ , intermediate lava viscosities of  $\eta \approx 3 \times 10^5 \text{ Pa s}$ , and very short durations of the effusion process of only 3–5 months. One should keep in mind, however, that the employed rheologic model may not be fully appropriate for lunar cones, since it does not account for explosive eruptions. The rheologic parameters of the small and relatively steep mare domes M8 and M9 resemble those of the lunar cones MC1, SC1, and SC2. They have formed out of similarly viscous lava with  $\eta \approx 10^6 \text{ Pa s}$ . Their larger size is due to somewhat higher effusion rates and longer durations of the effusion process between 1 and 1.5 years.

For the examined four fields of lunar mare domes, we were able to show that lava viscosity decreases exponentially with increasing  $R_{415}/R_{750}$  spectral ratio and thus  $\text{TiO}_2$  content (Fig. 13). A linear fit to the  $(R_{415}/R_{750}, \lg \eta)$  data points yields the relation

$$\lg \eta = -33.1(R_{415}/R_{750}) + 25.8, \quad (14)$$

where the moderate correlation coefficient of 0.65 illustrates that lava viscosity may be dominated by factors apart from  $\text{TiO}_2$  content, e.g., by the temperature of the lava during effusion. But even if the  $\text{TiO}_2$  content were strongly correlated with lava viscosity, the relatively weak correlation between  $R_{415}/R_{750}$  ratio and  $\text{TiO}_2$  content pointed out by Gillis and Lucey (2005) and outlined in some detail in Section 5.2.1 could explain the merely modest correlation between  $R_{415}/R_{750}$  ratio and lava viscosity observed in Fig. 13. However, most viscosity values estimated for mare domes in other lunar regions, lunar cones, and the Gruithuisen highland domes, for which we adopted the values for the lava viscosity reported by Wilson and Head (2003), fit well into the established empirical relation (14).

The values for the lava viscosities found in our data set span a range of six orders of magnitude, approximately from  $10^2$  to  $10^9 \text{ Pa s}$ . In comparison, the lava that formed the Gruithuisen highland domes had viscosities around  $10^9 \text{ Pa s}$ , which is not far

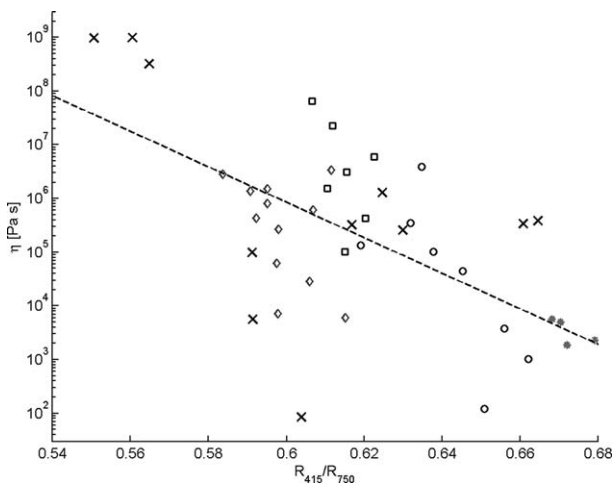


Fig. 13. Correlation between lava viscosity  $\eta$  and  $R_{415}/R_{750}$  spectral ratio. The dashed line represents the fit to our data derived from the four examined dome fields. Crosses denote the mare domes from other lunar regions, lunar cones, and Gruithuisen highland domes.

beyond the range we determined for lunar mare domes. Hence, unusual lava viscosity is probably not the primary reason for the peculiar 3D shapes of the Gruithuisen domes; they might rather be due to the low effusion rate, favoring steep slopes, the very long duration of the effusion process, yielding a high edifice volume, and the fact that lava effusion occurred over at least two distinct subsequent phases. The mare domes closest to the Gruithuisen highland domes in terms of their derived rheologic parameters are the edifices H5 and H6, which is also suggested by their morphometric properties (cf. Fig. 11c).

Consequently, the Gruithuisen highland domes on the one hand and the small and shallow class A mare domes in Mare Tranquillitatis, on the other hand, appear to represent endmembers of the dome formation process, spanning a broad continuous range of associated rheologic parameters: lava viscosities between  $10^2$  and  $10^9 \text{ Pa s}$ , effusion rates between about 25 and at least  $600 \text{ m}^3 \text{ s}^{-1}$ , and durations of the effusion process between a few weeks and about 40 years.

The discussion in this section may raise broad questions concerning the source regions of the various dome types and the corresponding implications for local and regional lunar volcanism, the reasons why certain types of lunar domes are concentrated in certain areas of the lunar surface, and which differences in the lunar interior are responsible for the different lunar dome properties observed on the surface. However, these questions go beyond the scope of this work and are therefore left for future studies.

## 7. Summary and conclusion

In this study we have examined four important fields of lunar mare domes in terms of the spectral properties and 3D shapes of the volcanic edifices. Accordingly, we have devised a classification scheme which is based on the extracted spectral and morphometric quantities. A physical interpretation of our data based on a rheologic model revealed the relevant range of lava viscosities, effusion rates, and durations of the effusion process valid for dome formation.

Class A domes are small and shallow and formed by high- $\text{TiO}_2$  lavas of low viscosity, erupting at high effusion rates over very short periods of time, resulting in edifices of low volume. Class B domes consist of lavas of intermediate to high viscosity and moderate  $\text{TiO}_2$  content, erupting at low to intermediate effusion rates. If the effusion process continues over a long period of time, steep flank slopes and high volumes may occur (class B<sub>1</sub>), while short periods of effusion result in shallower edifices of lower volume (class B<sub>2</sub>). Class C domes are formed out of low- $\text{TiO}_2$  (class C<sub>1</sub>) or high- $\text{TiO}_2$  (class C<sub>2</sub>) lavas building up edifices of large diameter but shallow flank slope. These flat shapes are due to low lava viscosities and high effusion rates. While classes A–C describe simple, likely monogenetic effusive domes, class D comprises the very complex, shallow but large and voluminous edifices Arago  $\alpha$  and  $\beta$ , which were most probably formed during several subsequent effusion stages. Lunar mare domes in other regions fit well into the established classification scheme, suggesting its general validity beyond the four dome fields examined in this study. Lunar

cones and highland domes, however, make up distinct groups of their own in our scheme.

We have shown that lava viscosity decreases with increasing  $R_{415}/R_{750}$  spectral ratio and thus  $\text{TiO}_2$  content of the soil, but the correlation is only moderate, which implies a possible influence of other parameters, most likely effusion temperature, on viscosity. At the same time it indicates that UV–vis color ratio may be controlled by other parameters apart from the  $\text{TiO}_2$  content of the soil. The viscosities determined for the four examined mare dome fields span a broad range of six orders of magnitudes, which is extended by a further order of magnitude by the viscosities of the lava that formed the Gruithuisen highland domes. Hence, we conclude that with respect to the rheologic parameters of the effusion process, the Gruithuisen highland domes and the shallow class A edifices in Mare Tranquillitatis represent endmembers of the formation process of effusive lunar domes, respectively.

Future work will include an extension of our analysis to a still larger number of effusive and intrusive mare domes, to more complex volcanic edifices like those encountered in the Marius Hills region, and to lunar domes situated inside or near large impact craters. Future high-resolution orbital data, e.g., from the Smart 1 spacecraft will allow for a more detailed analysis of the highly complex domes Arago  $\alpha$  and  $\beta$ . Such analyses may help to gain more detailed insight into the global and regional internal geologic processes responsible for the formation of the observed various types of lunar domes.

## Acknowledgments

We are grateful to Dr. C. Wood for fruitful discussions and his critical reading of the manuscript. We furthermore wish to express our thanks to the referees for their valuable comments and suggestions, and to C. Fattinanzi and K.C. Pau for contributing their CCD images shown in Figs. 12b and 12f, respectively.

## References

- Adams, J.B., McCord, T.B., 1970. Remote sensing of lunar surface mineralogy: Implication from visible and near infrared reflectivity of Apollo 11 samples. *Proc. Apollo Lunar Sci. Conf.* 11, 1937–1945.
- Arthur, D.W.G., 1962. Some systematic visual lunar observations. *Comm. Lunar Planet. Lab.* 4, 317–324.
- Ashbrook, J., 1961. Dimensions of the lunar dome Kies 1. *J. Ass. Lunar Planet. Obs.* 15 (1–2).
- Baldwin, R., 1963. *The Measure of the Moon*. Univ. of Chicago Press, Chicago, pp. 390–394.
- Basaltic Volcanism Study Project, 1981. *Basaltic Volcanism on the Terrestrial Planets*. Pergamon, New York.
- Baumgardner, J., Mendillo, M., Wilson, J.K., 2000. A digital high definition imaging system for spectral studies of extended planetary atmospheres. 1. Initial result in white light showing features on the hemisphere of Mercury unimaged by Mariner 10. *Astron. J.* 119, 2458–2464.
- Brungart, D.L., 1964. *The Origin of Lunar Domes*. M.Sc. thesis, Airforce Institute of Technology, Wright Patterson Air Force Base, OH.
- Burns, R.G., Parkin, K.M., Loeffler, B.M., Leung, I.S., Abu-Eid, R.M., 1976. Further characterization of spectral features attributable to titanium on the Moon. *Proc. Lunar Sci. Conf.* 7, 2561–2578.
- Bussey, B., Spudis, P., 2004. *The Clementine Atlas of the Moon*. Cambridge Univ. Press, Cambridge, UK.
- Cattermole, P., 1996. *Planetary Volcanism*, second ed. Wiley, Chichester.
- Charette, M.P., McCord, T.B., Pieters, C., Adams, J.B., 1974. Application of remote spectral reflectance measurements to lunar geology classification and determination of titanium content of lunar soils. *J. Geophys. Res.* 79 (11), 1605–1613.
- Chevrel, S.D., Pinet, P.C., Head, J.W., 1999. Gruithuisen domes region: A candidate for an extended non-mare volcanism unit on the Moon. *J. Geophys. Res.* 104 (E7), 16515–16529.
- Cook, A.C., Spudis, P.D., Robinson, M.S., Watters, T.R., Bussey, D.B.J., 1999. The topography of the lunar poles from digital stereo analysis. *Lunar Planet. Sci.* XXX. Abstract 1154.
- Dunkin, S.K., Heather, D.J., 1999. The Marius Hills volcanic complex: A stratigraphic study. *Lunar Planet. Sci.* XXX. Abstract 1180.
- Fielder, G., 1965. *Lunar Geology*. Lutterworth Press, London.
- Fink, J.H., Bridges, N.T., 1995. Effects of eruption history and cooling rate on lava dome growth. *Bull. Volcanol.* 57, 229–239.
- Gaddis, L.R., Staid, M.I., Tyburczy, J.A., Hawke, B.R., Petro, N.E., 2003. Compositional analyses of lunar pyroclastic deposits. *Icarus* 161, 262–280.
- Gillis, J.J., Lucey, P.G., 2005. Evidence that UV–vis ratio is not a simple linear function of  $\text{TiO}_2$  content for lunar mare basalts. *Lunar Planet. Sci.* XXXVI. Abstract 2252.
- Gillis, J.J., Lucey, P.G., Campbell, B.A., Hawke, B.R., 2005. Clementine 2.7  $\mu\text{m}$  data and 70-cm Earth-based radar data provide additional constraints for UV–vis-based estimates of  $\text{TiO}_2$  content for lunar mare basalts. *Lunar Planet. Sci.* XXXVI. Abstract 2254.
- Greeley, R., Batson, R.M., 1990. *Planetary Mapping*. Cambridge Univ. Press, Cambridge, UK.
- Hapke, B., 1993. *Theory of Reflectance and Emittance Spectroscopy*. Cambridge Univ. Press, Cambridge, UK.
- Head, J.W., Gifford, A., 1980. Lunar mare domes: Classification and modes of origin. *Moon Planets* 22, 235–257.
- Head, J.W., Wolf, U., Neukum, G., 2002. Stratigraphic sequence and ages in the Gruithuisen region of the Moon. *Lunar Planet. Sci.* XXXIII. Abstract 1619.
- Hiesinger, H., Head, J.W., Wolf, U., Jaumann, R., Neukum, G., 2003. Ages and stratigraphy of mare basalts in Oceanus Procellarum, Mare Nubium, Mare Cognitum, and Mare Insularum. *J. Geophys. Res.* 108 (E7), 5065–5091.
- Horn, B.K.P., 1989. Height and Gradient from Shading. MIT technical report 1105A. <http://people.csail.mit.edu/people/bkph/AIM/AIM-1105A-TEX.pdf>.
- Joshi, M.V., Chaudhuri, S., 2004. Photometric stereo under blurred observations. In: *Proc. 17th Int. Conf. on Pattern Recognition*, vol. 3., Cambridge, UK, pp. 169–172.
- Kuiper, G.P., 1961. *Orthographic Atlas of the Moon*. Univ. of Arizona Press, Tucson.
- Kuiper, G.P., Whitaker, E., Strom, R., Fountain, J., Larson, S., 1967. *Consolidated Lunar Atlas*. Lunar and Planetary Laboratory, Univ. of Arizona, Tucson, AZ.
- Lena, R., Wöhler, C., Phillips, J., Bregante, M.T., Pau, K.C., 2005a. A dome near crater Vendelinus, located at longitude +57.83° and latitude –15.74°. *The Lunar Observer*, May 2005, pp. 8–11.
- Lena, R., Fattinanzi, C., Phillips, J., Wöhler, C., 2005b. A study about a dome near Yerkes: Observations, measurements, and classification. *Selenology* 24 (2), 4–10.
- Lena, R., Pau, K.C., Phillips, J., Fattinanzi, C., Wöhler, C., 2005c. Lunar domes: A generic classification of the dome near Valentine, located at 10.26° E and 31.89° N. *J. Brit. Astron. Assoc.* 116 (1), 34–39.
- Lohse, V., Heipke, C., 2003. Derivation of digital terrain models by means of Multi-Image Shape-from-Shading: Results using Clementine images. In: *ISPRS Workshop: High Resolution Mapping from Space*, Hannover, Germany.
- Lucey, P.G., Blewett, D.T., Hawke, B.R., 1998. Mapping the FeO and  $\text{TiO}_2$  content of the lunar surface with multi-spectral imagery. *J. Geophys. Res.* 103 (E2), 3679–3699.
- McCord, T.B., Adams, J.B., 1973. Progress in optical analysis of lunar surface composition. *Moon* 7, 453–474.
- McCord, T.B., Charette, M.P., Johnson, T.V., Lebofsky, L.A., Pieters, C., Adams, J.B., 1972. Lunar spectral types. *J. Geophys. Res.* 77, 1349–1359.

- McCord, T.B., Pieters, C., Feierberg, M.A., 1976. Multi-spectral mapping of the lunar surface using ground-based telescopes. *Icarus* 29, 1–34.
- McEwen, A.S., 1985. Albedo and topography of Ius chasma, Mars. *Lunar Planet. Sci. XVI*, 528–529.
- McEwen, A.S., 1991. Photometric functions for photoclinometry and other applications. *Icarus* 92, 298–311.
- Melendrez, D.E., Johnson, J.R., Larson, S.M., Singer, R.B., 1994. Remote sensing of potential lunar resources. 2. High spatial resolution mapping of spectral reflectance ratios and implications for nearside mare TiO<sub>2</sub> content. *J. Geophys. Res.* 99 (E3), 5601–5619.
- Murase, T., McBirney, A.R., 1970. Viscosity of lunar lavas. *Science* 167, 1491–1493.
- Mursky, G., 1996. *Introduction to Planetary Volcanism*. Prentice–Hall, Upper Saddle River, NJ.
- Petrycki, J.A., Wilson, L., 1999. Volcanic Features and Age Relationships Associated with Lunar Graben. *Lunar Planet. Sci. XXX*. Abstract 1335.
- Pieters, C.M., 1978. Mare basalt types on the front side of the Moon: A summary of spectral reflectance data. *Lunar Planet. Sci. IX*, 2825–2849.
- Pike, R.J., 1978. Volcanoes on the inner planets: Some preliminary comparisons of gross topography. *Lunar Planet. Sci. IX*, 3239–3273.
- Pike, R.J., Clow, G., 1981. Revised classification of terrestrial volcanoes and catalogue of topographic dimensions, with new results of edifice volume. U.S. Geological Survey Open-File Report 81-1038.
- Press, W.H., Teukolsky, S.A., Vetterling, W.T., Flannery, B.P., 1992. *Numerical Recipes in C*. Cambridge Univ. Press, Cambridge, UK.
- Rajmon, D., Spudis, P., 2001. Distribution and stratigraphy of basaltic units in Mare Tranquillitatis. *Lunar Planet. Sci. XXXII*. Abstract 2156.
- Schürmann, J., 1996. *Pattern Classification*. Wiley–Interscience, New York.
- Smith, E.I., 1974. Rümker Hills: A lunar volcanic dome complex. *Moon* 10, 175–181.
- Spera, F.J., 2000. Physical properties of magma. In: Sigurdsson, H. (Ed.), *Encyclopedia of Volcanoes*. Academic Press, San Diego.
- Spudis, P., 1993. *The Geology of Multi-Ring Impact Basins*. Cambridge Univ. Press, Cambridge, UK.
- Staid, M.I., Pieters, C.M., Head, J.W., 1996. Mare Tranquillitatis: Basalt emplacement history and relation to lunar samples. *J. Geophys. Res.* 101 (E10), 213–227.
- Viegas, R., Lena, R., Bregante, M.T., 2005. A study about two cones near Milichius. *Selenology* 24 (2), 13–15.
- Warell, J., 2004. Properties of the Hermean regolith. IV. Photometric parameters of Mercury and the Moon contrasted with Hapke modeling. *Icarus* 167 (2), 271–286.
- Weitz, C.M., Head, J.W., 1999. Spectral properties of the Marius Hills volcanic complex and implications for the formation of lunar domes and cones. *J. Geophys. Res.* 104 (E8), 18933–18956.
- Wenker, A., 1999. *Geologic Map of the Near Side of the Moon*, based on the 1971 version by Don E. Wilhelms and John F. McCauley. USGS, Flagstaff, AZ.
- Westfall, J., 1964. A generic classification of lunar domes. *J. Ass. Lunar Planet. Obs.* 18 (1–2), 15–20.
- Whitford-Stark, J.L., Head, J.W., 1977. The Procellarum volcanic complexes: Contrasting styles of volcanism. *Lunar Planet. Sci. VIII*, 2705–2724.
- Wilhelms, D.E., 1964. A photometric technique for measurement of lunar slopes. In: *Astrogeologic Studies, Annual Progress Report, Part D: Studies for Space Flight Program*. USGS preliminary report, pp. 1–12.
- Wilhelms, D.E., 1987. *The geologic history of the Moon*. USGS Prof. Paper 1348.
- Wilhelms, D.E., McCauley, J.F., 1971. *Geologic Map of the Near Side of the Moon*. USGS, Flagstaff, AZ.
- Williams, D.A., Fagents, S.A., Greeley, R., 2000. A reassessment of the emplacement and erosional potential of turbulent, low viscosity lavas on the Moon. *Lunar Planet. Sci. XXXI*. Abstract 1102.
- Wilson, L., Head, J.W., 2003. Lunar Gruithuisen and Mairan domes: Rheology and mode of emplacement. *J. Geophys. Res.* 108 (E2), 5012–5018.
- Wöhler, C., Hafezi, K., 2005. A general framework for three-dimensional surface reconstruction by self-consistent fusion of shading and shadow features. *Pattern Recogn.* 38 (7), 965–983.
- Wood, C.A., 1979. Monogenetic volcanoes of the terrestrial planets. *Lunar Planet. Sci. X*, 2815–2840.